

Mutual Interactions Between a Thin Flexible Panel and Supersonic Flows

Himakar Ganti,^{1,2} Luis Bravo,³ Anindya Ghoshal,³ and Prashant Khare^{1,2}

¹*Department of Aerospace Engineering, University of Cincinnati, Cincinnati, OH 45221-0070*

²*Hypersonics Laboratory, Digital Futures, University of Cincinnati, Cincinnati, OH 45206*

³*Army Research Directorate, DEVCOM Army Research Laboratory, Aberdeen Proving Ground, MD, 21005*

(*Electronic mail: Prashant.Khare@uc.edu)

(Dated: 16 January 2025)

This paper discusses the mutual interactions between a thin flexible aluminum plate and supersonic flow using two-dimensional (2D) numerical simulations. Calculations are performed using an open source library, SU2, that solves partial differential equations governing fluid and structural dynamics. The configuration considered in this research effort is based on an experiment in which a thin flexible panel of 1.02 mm with a 50.8 mm overhang at the outer edge of a backward facing step is exposed to Mach 2 flow. The computational framework was first validated against measurements for both the initial transients of 10 ms and the fully started conditions at 0.4 s. Then, numerical studies were performed to analyze the fluid-structure interactions at 4 different Mach numbers between 0.5 and 3. The flow behavior revealed distinct phenomena, including shear layer separation for subsonic and transonic flows, and a fully enclosed recirculation region under the overhang in supersonic cases. The time-averaged flow field identified potential temperature hotspots during the initial transients, which intensified as time evolved. For Mach 0.50, the amplitude of the thin panel oscillations increased as the flow transitioned from transient to steady-state conditions. In the transonic case ($M = 0.95$), the oscillation amplitude became significantly larger, potentially leading to resonant behavior and structural failure (we did not model failure). However, in the supersonic cases, the oscillations stabilized and were sustained after the initial transients. The research quantitatively identifies the influence of the Mach number on the fluid-structure interaction phenomena, which affect pressure loads and the development of thermal hotspots, which are crucial elements in engineering design.

I. NOMENCLATURE

FSI	Fluid-Structure-Interaction
2D	2-dimensional
3D	3-dimensional
SWBLI	shock-wave boundary-layer interactions
ROM	reduced order modeling
POD	Proper Orthogonal Decomposition
SPOD	Spectral Proper Orthogonal Decomposition
RANS	Reynolds-Averaged Navier-Stokes
LES	Large Eddy Simulations
WMLES	Wall Modeled Large Eddy Simulations
SGS	Sub-Grid-Scale
SM	Smagorinsky Model
CM	Clark Model
DCM	Dynamic Clark Model
DNS	Direct Numerical Simulation
VSGSM	Vreman Sub-Grid-Scale Model
DDES	Delayed Detached Eddy Simulation
SA	Spalart-Allmaras
FEM	Finite Element Method
FVM	Finite Volume Method
MUSCL	Monotonic Upwinding Centered Scalar Conservation Law
FGMRES	Flexible Generalized Minimum Residual
FFT	Fast Fourier Transform

II. INTRODUCTION

Computational investigation of mutual interaction between structures and fluids (FSI), sometimes also referred to as aeroelasticity, has been a topic of interest for many decades¹⁻⁴, especially in weakly compressible or incompressible low-speed flows relevant to a range of applications, including physiological flows⁵⁻⁸, turbines⁹ and flow in pipes¹⁰. There is also a rich literature that details aeroelastic interactions in aircraft and helicopters¹¹⁻¹⁵ that move primarily in the subsonic/transonic flow regime. Recent interest in supersonic and hypersonic flight has not only led to increased research activities on high-speed fluid dynamics¹⁶⁻¹⁸ and gaseous/liquid-fueled combustion processes¹⁹⁻²⁶, but also spurred FSI research in the supersonic and hypersonic flow regime, and several experiments and computational studies have been conducted to investigate this phenomenon²⁷⁻²⁹. In particular, canonical configurations, such as supersonic/hypersonic flow over thin flexible panels that resemble the interactions between high-speed flow and the inlet of scramjet engines, have been a popular area of investigation in the recent past because of their importance to practical systems of interest; a brief summary of the literature that discusses these studies is summarized in the following paragraphs. This is also the topic of the current article, which details the interactions between a thin panel and a range of flow conditions from sub-, trans-, to supersonic flow. Unlike many studies in the past that investigated laminar-flow conditions while investigating FSI in supersonic-flow conditions, we took into account turbulent flow using a wall-modeled large-eddy simulation (WMLES) framework, loosely coupled with a structural solver to eluci-

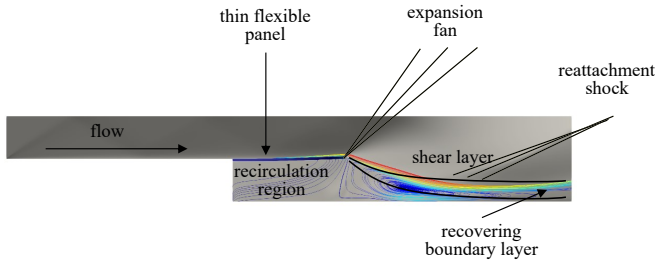


FIG. 1: Schematic of the experimental configuration used to study the interactions between a cantilevered panel and supersonic flows.

date the governing physical processes in both the fluid and solid domains.

As mentioned in the previous paragraph, much progress has been made over the past decade in understanding the fundamental FSI phenomenon related to high-speed flows through well-controlled experiments. These experiments can generally be classified into two kinds depending on how the structure is held in place as it interacts with supersonic/hypersonic flow: (1) cantilevered rigid compliant panel^{30–33}, and (2) edge-clamped panel^{34–44}. While the first configuration consists of shock-free flow parallel to the cantilevered panel (shocks may appear as a result of geometric or boundary/shear-layer effects), the second configuration is designed to have a shock impinge on the surface of the panel; thus both setups investigate slightly different processes. This research effort focuses on the former and investigates the detailed flow and structural dynamics.

The experimental setup of Bojan, Dutton, and Elliott³³ represents the interactions between high-speed flow and a cantilevered-compliant panel. In this experiment, a schematic of which is shown in figure 1, a 50 mm aluminum panel of 1.02 mm width is attached as a cantilever and exposed to a flow at a Mach number of 2.11. This canonical configuration encompasses the rich physics relevant to practical high-speed vehicles, including but not limited to shock and expansion waves, shear layers, shock-boundary layer interactions, recirculation zones, and the mutual interactions between these processes and the solid structure. High-speed digital imaging and particle image velocimetry (PIV) were used to capture flow and structural responses. The flow data were time-averaged for both transient and fully started conditions, while the thin panel’s behavior was documented through the time evolution of the beam’s displacement. Oscillatory behavior was monitored using pressure probes placed in the separated recirculation region.

Brouwer *et al.*⁴¹ conducted experiments on an edge-clamped, thin compliant panel in a Mach 1.5 to 3.0 supersonic wind tunnel, schematically shown in figure 2. The panel featured a pressure cavity on the opposite side of the flow tunnel, equipped with multiple transducers along its length to measure pressure and temperature profiles. The turbulent supersonic flow excited the panel, and a shock generator induced shock impingement at various points along the span. The study provides a detailed analysis of the panel’s behav-

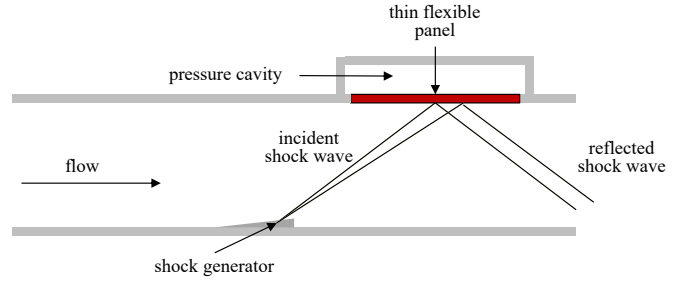


FIG. 2: Schematic of the experimental configuration used to study the interactions between an edge-clamped panel and supersonic flows.

ior, utilizing multiple pressure and temperature measurements and modal decomposition to determine mode shapes and oscillation frequencies. As a follow-up to this study, recently, Brouwer *et al.*⁴⁴ conducted numerical simulations using the Reynolds-averaged Navier-Stokes (RANS) approach and developed a reduced-order model of the structural behaviors of the thin plate. Although the mean transport fields effectively captured bulk flow properties, the authors highlighted that higher-fidelity scale-resolving models are necessary to accurately capture boundary layer interactions and improve predictions of pressure loading on the panel.

To fully grasp such interactions in question, it is essential to simultaneously measure or model the key physical processes involved, such as structural dynamics, including buckling, conjugate heat transfer, highly compressible turbulent flow, thermochemical non-equilibrium (relevant in hypersonic flow), and shock-boundary layer interactions. Moreover, the complexity of investigating these phenomena is heightened because of the broad range of lengths (from sub-micrometer to meter) and time scales (from nanosecond to second) that dictate them. Although several studies have focused on oscillation, buckling, and deflection dynamics under supersonic^{34,41} or hypersonic^{30–32,37,38} conditions based on cantilevered or edge-clamped configurations, most of these studies, irrespective of the mode of investigation (experimental measurements or computations), discussed the structural deformation modes, primarily based on pressure and/or thermal loading (primarily for hypersonic flow conditions) loading due to the flow conditions.

A common limitation in experimental or numerical research on this topic has been the reliance on time-averaged data for fluid and solid domains, overlooking the dynamics and turbulent flow. In this paper, we attempt to address these gaps by conducting computations based on unsteady wall-modeled large eddy simulations to investigate the interactions between a cantilevered thin beam as it is exposed to a range of Mach numbers from 0.5 to 3.

The article is organized as follows: the equations that govern the fluid and structural dynamics are described in detail, including the subgrid-scale (SGS) models that we use for turbulence closure. This is followed by a detailed validation and grid sensitivity study to establish the appropriateness and accuracy of our numerical framework. To do so, we simulate the

experiment of Bojan, Dutton, and Elliott³³ and compare our results with measurements during both the initial transients and the fully started conditions. For this case, the flow Mach number is 2.11. Next, mutual interactions between flow and structure at a range of flow Mach numbers in the subsonic ($M = 0.5$), transonic ($M = 0.95$), and supersonic ($M = 2.11$ and 3.0) regimes are discussed. In the last section, we summarize the major conclusions from the study.

III. GOVERNING EQUATIONS AND NUMERICAL METHODS

The SU2 multiphysics library⁴⁵ is used to investigate the FSI phenomenon described above. In this section, the equations that govern the processes in the fluid and solid domains, their interfacial interactions, and associated numerical methods are described.

A. Fluid Domain

The Favre averaged conservation equations for mass, momentum and energy are given by:

$$\begin{aligned} \frac{\partial \bar{\rho}}{\partial t} + \frac{\partial \bar{\rho} \tilde{u}_i}{\partial x_i} &= 0 \\ \frac{\partial \bar{\rho} \tilde{u}_i}{\partial t} + \frac{\partial \bar{\rho} \tilde{u}_i \tilde{u}_j}{\partial x_j} &= -\frac{\partial \bar{p}}{\partial x_i} + \frac{\partial (\bar{\tau}_{ij} - \tau_{ij}^{SGS})}{\partial x_i} \\ \frac{\partial \bar{\rho} \tilde{E}}{\partial t} + \frac{\partial [(\bar{\rho} \tilde{E} + \bar{p}) \tilde{u}_i]}{\partial x_i} &= \frac{\partial (-\bar{q}_i + \tilde{u}_j \bar{\tau}_{ji} - \sigma_i^{SGS} - H_i^{SGS})}{\partial x_i} \end{aligned} \quad (1)$$

where ρ is the density, u_i is the velocity along the direction x_i , p is the pressure. The filtered mean shear stress is $\bar{\tau}_{ij}$, and \bar{q}_i is the heat flux or thermal energy flux. The filtered total energy, \tilde{E} is the sum of filtered internal energy, \bar{e} , resolved kinetic energy, $\frac{1}{2} \tilde{u}_i \tilde{u}_i$, and the SGS kinetic energy, k^{SGS} are given as

$$\begin{aligned} \tilde{E} &= \bar{e} + \frac{1}{2} \tilde{u}_i \tilde{u}_i + k^{SGS} \\ k^{SGS} &= \frac{1}{2} (\overline{u_i u_i} - \bar{u}_i \bar{u}_i) \end{aligned} \quad (2)$$

Conduction, q_i is modeled using Fourier's law, where the thermal conductivity is calculated using the local temperature-dependent molecular viscosity and a Prandtl number of 0.72. The temperature-dependent dynamic viscosity is evaluated using the Sutherland model. For a reference temperature T_0 , reference viscosity μ_0 , and Sutherland constant S_μ , the Sutherland model for dynamic viscosity is:

$$\mu = \mu_0 \left(\frac{T}{T_0} \right)^{3/2} \left(\frac{T_0 + S_\mu}{T + S_\mu} \right) \quad (3)$$

The unclosed SGS terms appearing in the Favre averaged equations are the SGS stress $\tau_{i,j}^{SGS}$, the energy flux $H_{i,j}^{SGS}$. The

term $\sigma_{i,j}^{SGS}$ is obtained from the correlations of the velocity field with the viscous stress tensor.

$$\begin{aligned} \tau_{i,j}^{SGS} &= (\overline{\rho u_i u_j} - \bar{\rho} \tilde{u}_i \tilde{u}_j) \\ H_{i,j}^{SGS} &= (\overline{\rho \tilde{E} u_i} - \bar{\rho} \tilde{E} \tilde{u}_i) + (\overline{p u_i} - \bar{p} \tilde{u}_i) \\ \sigma_{i,j}^{SGS} &= (\overline{u_j \tau_{ij}} - \tilde{u}_j \bar{\tau}_{ij}) \end{aligned} \quad (4)$$

$\tau_{i,j}^{SGS}$ is closed using the the Vreman SGS Model (VSGSM)⁴⁶, given by:

$$\begin{aligned} \tau_{ij} &= -2\nu_e S_{ij} + \frac{1}{3} \tau_{kk} \delta_{ij} \\ \bar{S}_{ij} &= \frac{1}{2} \left(\frac{\partial u_j}{\partial x_i} + \frac{\partial u_i}{\partial x_j} \right) \\ \nu_e &= c \sqrt{\frac{B_\beta}{\alpha_{ij} \alpha_{ij}}} \\ \alpha_{ij} &= \partial_i u_j = \frac{\partial u_j}{\partial x_i} \\ \beta_{ij} &= \Delta_m^2 \alpha_{mi} \alpha_{mj} \end{aligned} \quad (5)$$

$$B_\beta = \beta_{11} \beta_{22} + \beta_{11} \beta_{33} + \beta_{22} \beta_{33} - \beta_{12}^2 - \beta_{13}^2 - \beta_{23}^2$$

where the model constant, c , is related to the Smagorinsky constant⁴⁷, C_s , as $c \approx 2.5 C_s^2$. This model needs only a local filter width and first-order derivatives of the velocity field. α is the matrix of derivatives of the filtered velocity, \bar{u} , the filter width is Δ_m , B_β is an invariant of the tensor, β . This implies that if $\Delta_i = \Delta$ then $\beta = \Delta^2 \alpha^T \alpha$. Although we realize the importance of $H_{i,j}^{SGS}$ and $\sigma_{i,j}^{SGS}$, especially for highly compressible flows, because of the second to third order effects of these terms on structural dynamics, in this study we neglect these SGS terms.

To model the boundary layer, the LES framework described above is coupled to the algebraic wall stress model of Reichardt⁴⁸. However, we realize that this and other such models (e.g., Spalding *et al.*⁴⁹, Musker⁵⁰) start to break down when Mach numbers are high; since this study is limited to Mach numbers of up to 3, we use the model of Reichardt⁴⁸ in this research investigation. For higher Mach-number flows, the topic of our upcoming manuscript, we are implementing the Van Driest transformation in conjunction with one of the aforementioned wall models to model the boundary layer accurately.

B. Solid Domain

The solid domain is governed by elasticity equations for large deformations⁵¹, implemented in the SU2 library by Sanchez *et al.*⁵². A short description of the Venant-Kirchhoff model is given here. This model can handle large deformations of an isotropic and homogeneous solid in a Lagrangian framework. The elasticity equations are solved in differential form as:

$$\rho_s \frac{\partial^2 \mathbf{u}}{\partial t^2} = \nabla \cdot (\mathbf{F} \cdot \mathbf{S}) + \rho_s \mathbf{f} \quad (6)$$

The boundary conditions are imposed on the interface degrees of freedom, which are categorized into essential (e) and natural (n) conditions. The essential boundary conditions impose the solution $u_{s,e}$ on the interface nodes and later apply the tractions $\lambda_{s,n}$ on the boundary. The boundary conditions for the solid are:

$$\begin{cases} \mathbf{u}_s = \mathbf{u}_{s,e} & \text{on } \Gamma_{s,e} \\ \boldsymbol{\sigma}_{s,n_s} = \boldsymbol{\lambda}_{s,n} & \text{on } \Gamma_{s,n} \end{cases} \quad (7)$$

where ρ_s is the density of the solid, \mathbf{u} are the displacements of the solid, t is the time, \mathbf{F} is the deformation gradient of the material and f is the volume force. \mathbf{S}^{PK} is the second Piola-Kirchhoff stress tensor:

$$S_{ij}^{\text{PK}} = \lambda_s E_{kk} \delta_{ij} + 2\mu_s E_{ij} \quad (8)$$

δ_{ij} is the Kronecker delta, λ and μ are Lamé's constants. The Lagrangian stress tensor, E_{ij} , is given as:

$$E_{ij} = \frac{1}{2} \left(\frac{\partial u_i}{\partial x_j} + \frac{\partial u_j}{\partial x_i} \right) + \frac{1}{2} \frac{\partial u_k}{\partial x_i} \frac{\partial u_k}{\partial x_j} \quad (9)$$

Lamé's constants λ_s and μ_s are given in terms of Young's modulus, Y , and the Poisson's ratio, ν_s , as:

$$\mu_s = \frac{Y}{2(1+\nu_s)}, \quad \lambda_s = \frac{Y\nu_s}{(1+\nu_s)(1-2\nu_s)} \quad (10)$$

For further details, the reader is referred to the literature^{51,52}.

C. Fluid-Solid Interfacial Conditions and Numerical Methods

The fluid and solid domain interface will have imposed boundary conditions for a physically correct flow. For a viscous fluid flow, the non-slip condition specifies that the fluid velocity at the boundary must be the same as the boundary velocity itself^{52,53}. Continuity is imposed at the interface as:

$$\mathbf{u}_f = \mathbf{u}_s = \mathbf{u}_\Gamma \quad (11)$$

Imposing equilibrium at the interface leads to the following condition:

$$\boldsymbol{\lambda}_f + \boldsymbol{\lambda}_s = 0 \quad (12)$$

$\boldsymbol{\lambda}_f$ is the fluid traction which maps the fluid displacements on the interface with a Dirichlet-to-Neumann non-linear operator, F_f , for the fluid domain as:

$$\boldsymbol{\lambda}_f = F_f \left(\mathbf{u}_{\Gamma_f} \right) \quad \text{on } \Gamma_{f,i} \quad (13)$$

and $\boldsymbol{\lambda}_s$ is the solid traction and is related to the solid displacements with a Dirichlet-to-Neumann non-linear operator, F_s , for the solid-structural domain as:

$$\boldsymbol{\lambda}_s = F_s \left(\mathbf{u}_{\Gamma_s} \right) \quad \text{on } \Gamma_{s,n} \quad (14)$$

Above equations lead to a Steklov-Poincaré equation which can be rewritten as a fixed point equation,

$$\begin{aligned} F_f(\mathbf{u}_\Gamma) + F_s(\mathbf{u}_\Gamma) &= 0 \\ F_s^{-1}(-F_f(\mathbf{u}_\Gamma)) &= \mathbf{u}_\Gamma \end{aligned} \quad (15)$$

The partitioning algorithm then consists of a single solution to the Dirichlet-to-Neumann operator for the fluid domain, and an inverse Neumann-to-Dirichlet operator for the solid domain per time step.

Note that while conjugate heat transfer is important, especially at elevated Mach numbers, in this manuscript to isolate aerodynamic loads from thermal loads, we do not consider heat transfer from the fluid to any solid walls in the computational domain. All walls, including the thin panel, are maintained at an isothermal temperature of 300 K. The combined effect of thermal and aerodynamic loading on fluid structure interactions will be discussed in a subsequent manuscript.

The fluid domain was spatially discretized using a first-order ROE scheme; an approximate Riemann solver in a Finite-Volume formulation. Time-marching was achieved with a second-order, dual-time stepping scheme. Turbulence was modeled with the Vreman SGS model. The key parameter for WMLES is the distance from the wall where the algebraic logarithmic wall function should be applied. In our simulations, the log-law was applied at y^+ of 5, and was fixed for all simulations. A flexible generalized minimal residual method, (FGMRES), is used for the linear solver iterator of the fluid domain. The fluid domain had non-reflecting boundary conditions, and forces due to pressure along the interface are transferred to the solid domain for loading. The solid domain used simple loading to replicate pressure, and the elasticity equations are solved with a first-order finite element Newton-Raphson scheme. The Newmark algorithm is used for time integration. A conjugate-gradient method was used for iterating the linear solver iterator for the solid domain solutions. Due to the significant differences between the time scales of the fluid and the structural dynamics, the equations that describe the two domains are loosely coupled; i.e., the structural solver is called once for each time step in the fluid domain. Each of the two solvers uses a second-order dual time-stepping technique, with 101 inner iterations per outer iteration.

IV. MODEL VALIDATION

Before using the computational framework to elucidate the fluid and structural dynamics of a thin flexible panel as it interacts with subsonic, transonic, and supersonic flows, it is first validated against experiments of Bojan, Dutton, and Elliott³³. The experimental setup (see figure 1) and instrumentation was described in Section II. Bojan, Dutton, and Elliott³³ organized their measurements and associated statistics in two categories: first 10 ms and then for up to 0.4 s. The operating conditions and material properties for both air and aluminum are tabulated in table I. The natural frequency and the first three harmonics of the panel are 303, 389, 661 and 1159 Hz, respectively. In addition to the frequency of oscillation of the

panel, several flow characteristics were identified, including a recirculation region underneath the plate; an expansion fan at the outer top edge of the plate; a shear layer that originates at the outer edge of the plate and descends to the bottom wall with boundary layer recovery further downstream; a reattachment shock attached to the top of the shear layer downstream of the plate – these are shown in figure 1. Depending on the flow Mach number, all or some features (not described above) are expected to be observed.

TABLE I: Fluid and solid properties used to simulate the experiment of Bojan, Dutton, and Elliott³³.

Air		
Total Pressure	<i>kPa</i>	277.6
Total Temperature	<i>K</i>	277
Mach		2.11
Freestream Pressure	<i>kPa</i>	29.885
Viscosity at 273 K	<i>N-s/m²</i>	1.173×10^{-5}
Reynolds Number		3927788
Thin Aluminum Panel		
Density	<i>kg/m³</i>	2700
Elasticity	<i>GPa</i>	72.0
Poisson's Ratio		0.33
Thickness	<i>mm</i>	1.02
Length	<i>mm</i>	50.8

A. Grid Sensitivity Study

Before comparing the computational results with measurements, a grid sensitivity study was conducted. Three different unstructured meshes were generated, details of which are listed in table II. All three grids are designed to be refined near the walls of the thin panel and then stretch to an isotropic grid in the core flow region. The minimum grid size in each case is 10 μm , near the walls. The grid in the core region differs in each case; 200, 300 and 400 μm for L2, L3 and L4, respectively. Figure 3 shows an example of the discretized domain, where the yellow color represents the refinement region, stretching from the smallest to the largest, while the green region represents the isotropic grid away from the wall. The mesh for the solid domain is unstructured and uniform with a size of 100 μm for all three cases.

Mesh deformation is handled with a pseudostructural approach as a linear-elasticity problem with boundary conditions that determine the displacements of the interior nodes, Sanchez *et al.*⁵². The interface displacements are set as structural displacements and the boundaries are set as static. To prevent elements from having negative areas, the stiffness of each cell is set independently as an inverse function of the area or volume of the elements and Lamé's constants are determined from the area or volume.

The results of the grid sensitivity analysis are discussed in terms of time-averaged flow and structural behaviors over 0.4 s.

Figure 4 shows the time-averaged density contours overlaid by time-averaged streamlines for cases L2, L3 and L4.

TABLE II: Details of the grids for both fluid and solid domains for the grid sensitivity analysis.

Fluid Domain				
Grid	Grid Size, μm		Number of	
	Maximum	Minimum	Elements	Grid Points
L2	200	10	1.92×10^6	980×10^3
L3	300	10	1.20×10^6	620×10^3
L4	400	10	865×10^3	452×10^3
Solid Domain				
Solid	100		13.4×10^3	7.2×10^3

All three grids are able to capture the expansion fan, reattachment shock, shear layer reattachment, and recovering boundary layer. The recirculation region is also captured by the three grids; however, the vortex structure attached to the outside lower edge of the thin-flexible plate and just below the shear layer captured using L2 and L3 are very similar, while that from L4 differs from the other two.

Figures 5a, b, c show the displacement of the tip of the panel with time. All three grids capture the initial transients in the first 0.2 s, which are then stabilized and sustained in amplitude from 0.2 to 0.4 s. The stabilized oscillations from the three grids beyond 0.2 s are shown in figure 5d. Note that the displacement of the tip is normalized by the height of the panel. Although there are clear differences in the amplitude when different grids are used, the frequency of oscillation calculated by taking the FFT is 367 Hz. So, while the detailed behaviors are dictated by the grid size, the characteristics do not change for grids L2-L4. Therefore, given that the flow features under the thin panel are going to be important as it oscillates, even though L3 is presumably sufficient to resolve them, since we intend to investigate flows up to Mach 3 (i.e., higher Reynolds number), we will use L2 for all cases described in the rest of this paper.

B. Comparison between Computations and Measurements

Figure 6 shows the instantaneous flowfield and panel deformation at 0.0, 2.0, 4.0, 6.0, 8.0, and 10 ms corresponding to the configuration described in the previous section. A shear layer is formed at the tip of the panel, which extends to the lower wall. As the panel oscillates, shown in the figures 6 a-f, the shear layer oscillates with it. Other flow features, such as the expansion fan when the panel moves downwards and the reattachment shock owing to the interactions between supersonic flow and the shear layer, are also observed. Tip vortices are formed due to the motion of the panel; the shear layer prevents them from convecting downstream. While all the vortices interact with the shear layer, the one that is furthest away from the wall stretches due to this interaction, eventually dissipating at the bottom wall. All these flow features were also observed in the experiment.

The qualitative time-averaged flow features observed in the experiments of Bojan, Dutton, and Elliott³³ were successfully captured by our calculations using the L2 grid – see figure

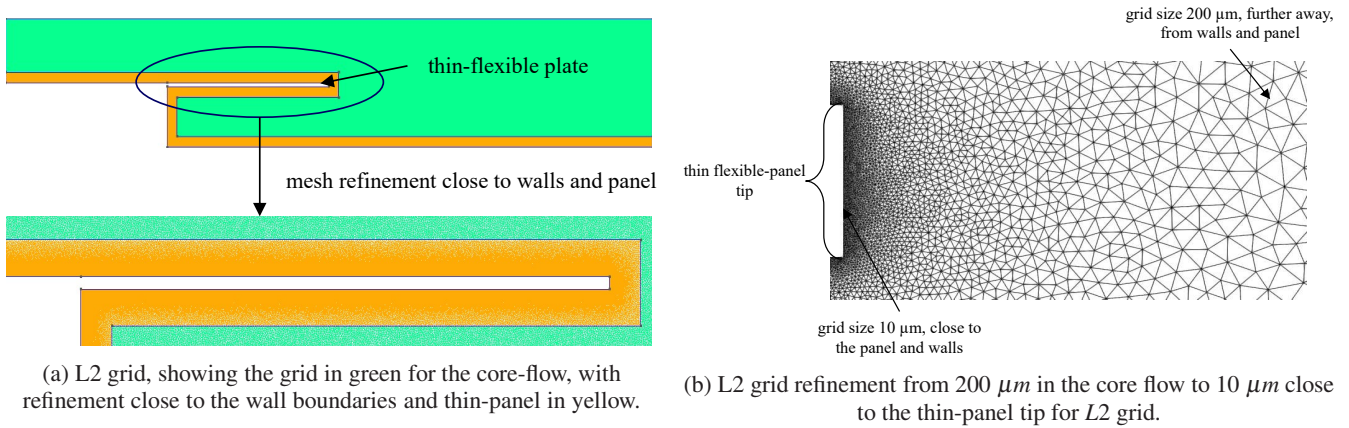


FIG. 3: L2 grid details, showing refinement close to the walls and thin-flexible panel.

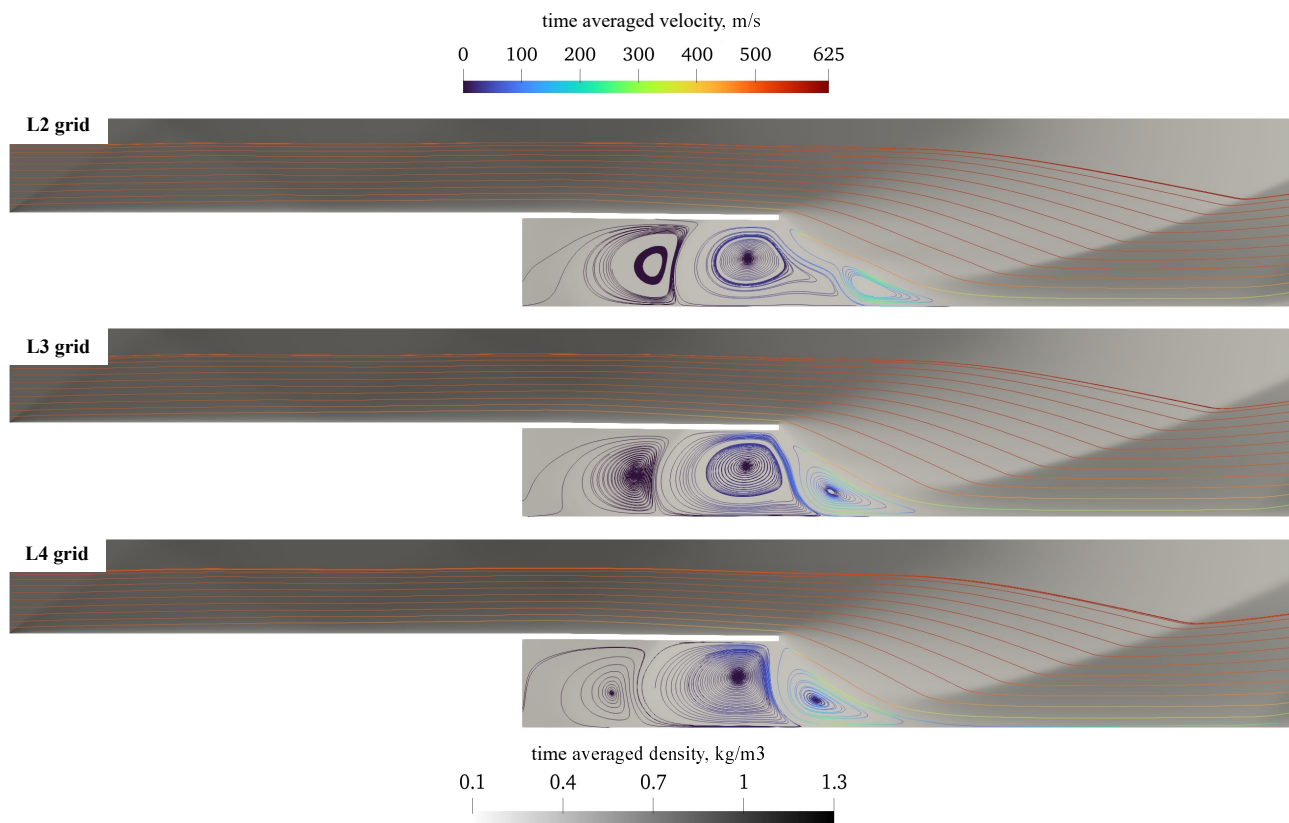
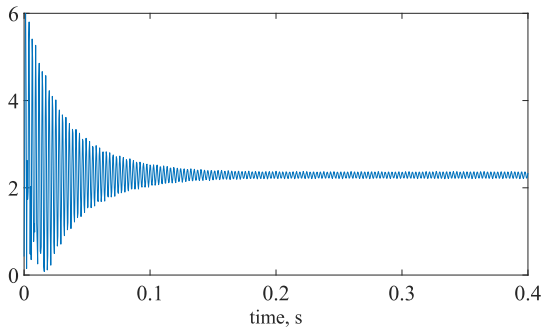
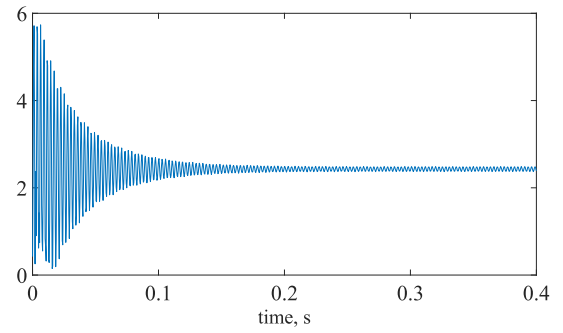
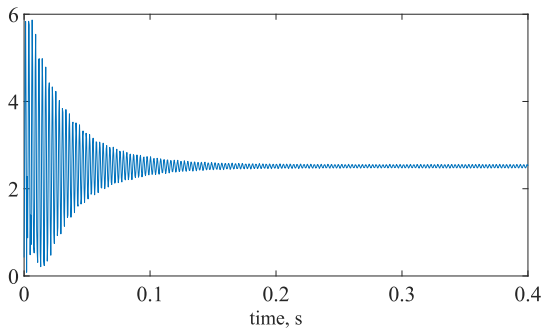
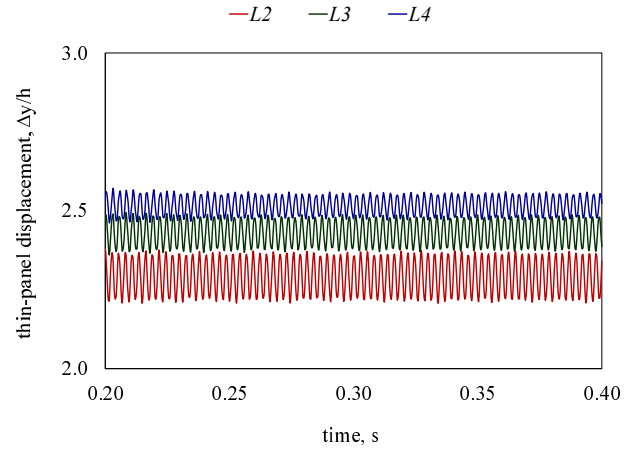


FIG. 4: Comparison of time averaged flow of the grids - L2, L3 and L4.

4. Quantitatively, we compare the panel tip displacement and the corresponding oscillation frequency measured in the experiment for the first 10 ms and the fully started conditions (described as the time after 10 ms up to 0.4 s). This comparison is shown in figure 7 for the first 10 ms. The displacement, Δ , is normalized by the thin-plate thickness, h .

The displacement amplitudes and phases compare well. The oscillation frequency calculated from this chart is 395 Hz, which is very close to the experimentally measured frequency of 397 Hz. After the initial transients, once the tip

displacements reach a stationary state between 0.2 to 0.4 s, the frequency of oscillation from our computations is 367 Hz, in good agreement with the measured frequency of 366 Hz. The details are shown in figure 8.

(a) displacement-time plot for $L2$ grid(b) displacement-time plot for $L3$ grid(c) displacement-time plot for $L4$ grid

(d) comparison of displacements from the three grids

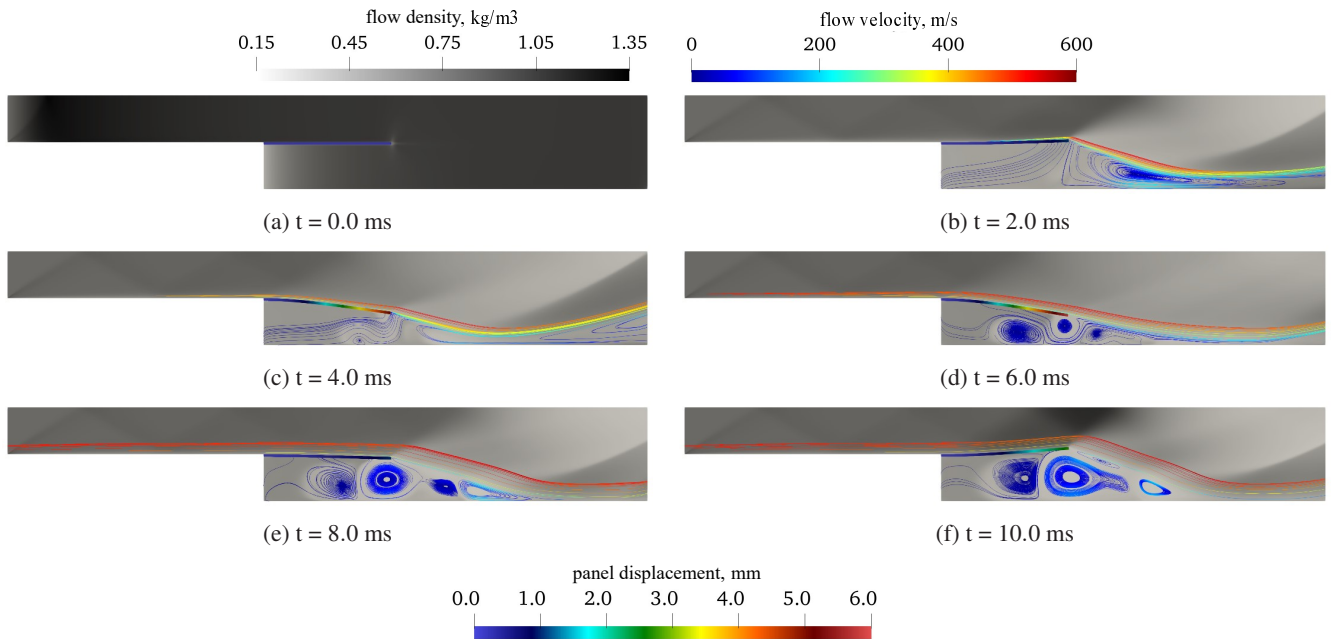
FIG. 5: Displacement-time plots and their comparison after initial transients are stabilized for the three grids, $L2$, $L3$ and $L4$.

FIG. 6: Temporal evolution of Ma 2.11 flow, showing velocity streamlines on density contours and compliant panel displacement for initial transient conditions.

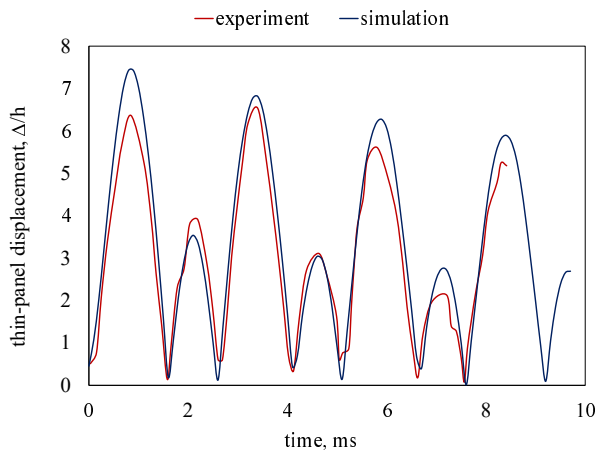
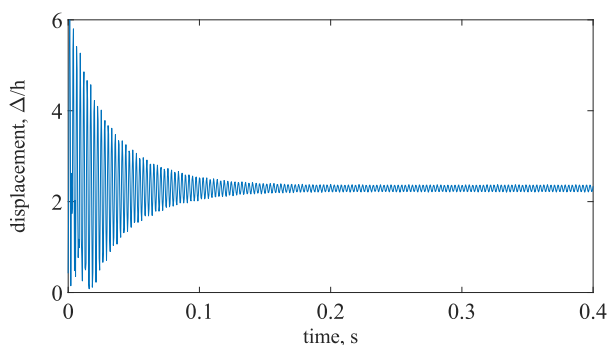
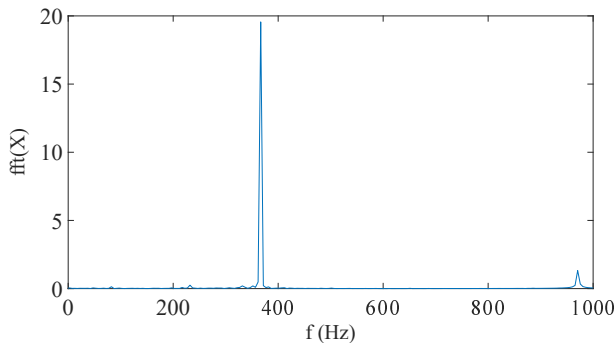


FIG. 7: Comparison of panel tip displacement between simulations and experiments³³ for the first 10 ms.



(a) time evolution of tip displacement



(b) FFT of tip displacement over time shown in figure 8a for $0.2 \leq t \leq 0.4$.

FIG. 8: Numerical simulation results for steady or fully started conditions.

V. EFFECT OF MACH NUMBER ON FLUID STRUCTURE INTERACTIONS

To identify similarities and differences in the FSI behaviors in sub-, trans- and supersonic flows, in addition to the validation case at Mach number 2.11, three additional simulations

were conducted at Mach numbers of 0.5, 0.95 and 3. The cases are set up such that the static temperature and pressures are 146.53 K and 29.89 kPa, respectively, at the entrance of the conduit. All cases use the L2 grid. In the next two subsections, we discuss the effect of Mach number on the flow and structural dynamics for the initial transients (time up to 10 ms) and the fully started conditions (times up to 0.4 s). These discussions will be based on time-averaged variables.

A. Initial Transient Conditions (up to 10 ms)

1. Flow Behaviors

Figure 9 shows the time averaged (over the first 10 ms) density and streamlines for the four Mach numbers mentioned in the previous paragraph. As shown in figures 9a and 9b, at subsonic and transonic speeds, the shear layer does not adhere to the bottom wall downstream of the thin plate. This leads to stretching the tip vortex along the shear layer in both cases. Prominent vortices, trapped under the plate are observed for the two supersonic flow cases. The behaviors of the shear layer are dictated by the movement of the panel. To explain these behaviors, consider the tip displacement for the four cases shown in figure 10. The displacements for Mach 0.50 and 0.95 show peaks at irregular intervals, whereas the displacements for Mach 2.11 and 3.00 look periodic. More importantly, the displacement amplitudes for the subsonic and transonic cases (up to 2 times the plate thickness) are at least 3-4 times smaller than those of the supersonic cases (up to 8 times the plate thickness). This is attributed to the higher fluid momentum for cases with higher Mach numbers leading to higher pressure loading on the plate. For Mach 2.11 and Mach 3.00, the displacement amplitude gradually decreases over time, indicating damping. These higher amplitudes of panel motion in case of higher Mach number flows lead to the motion of the shear layer, which when interacting with the boundary layer attaches to the bottom wall. This additionally enables the vortices formed at the plate's trailing edge to intensify and remain confined beneath the plate. These behaviors are absent for cases with Mach numbers of 0.5 and 0.95.

Another flow feature observed for the two supersonic cases is the weak shock train resulting from the interactions between the supersonic flow and the boundary layer; these are observed in the density contours in figures 9c and d.

Figures 11a-d show the temperature contours overlaid with streamlines. Note that because of a wide variation in the range of temperature and velocities, to capture flow structures, the legends are different for each case. Similar to the velocity boundary layer near all the walls described in the previous paragraph, a thermal boundary layer is also observed with the highest temperatures near the wall, owing to dissipation, decreasing to the core flow value. The Mach 0.5 flow is weakly compressible and, consequently, there is no significant change in the core flow temperature except near the wall. For higher Mach number cases, other flow features, such as shock and expansion waves lead to significant variations in the core region's temperature field. For example, near the trailing edge

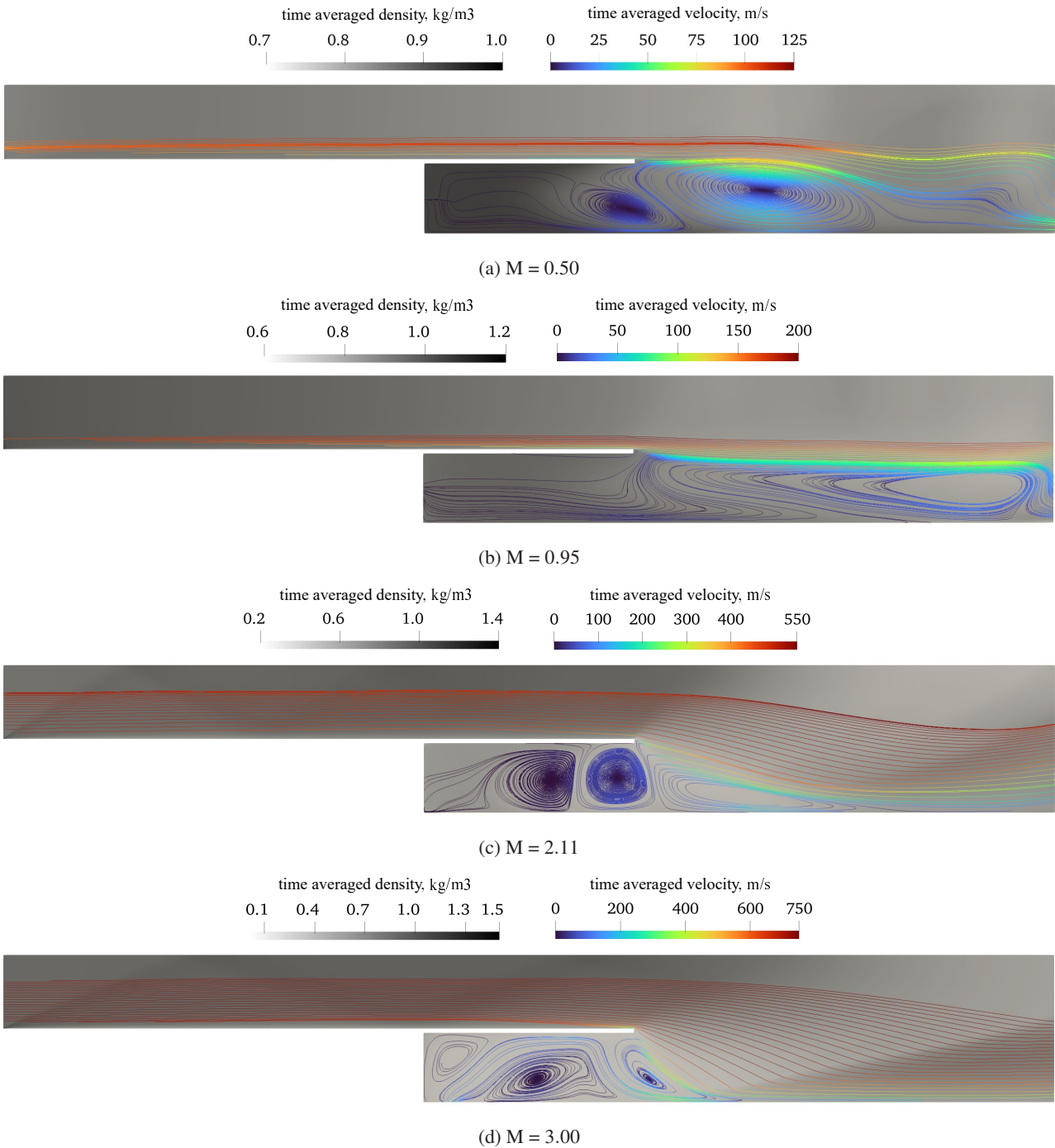


FIG. 9: Time-averaged density fields, overlaid with velocity streamlines for initial transient conditions.

of the panel, the temperature decreases across the expansion fan, and increases across the oblique shock waves, visible in figures 11c and d. Similar to the boundary, there is significant dissipation in the shear layer, especially for the higher Mach number flows where velocity gradients are significant, resulting in higher temperature field in that region.

2. Panel Deformation and Stresses

To understand the behavior of initial transient flow Mach number on the panel behavior, time averaged panel deformations are compared for the four cases in figure 12. A clear trend of increase in panel deformations with flow Mach number is observed. The deformation for the Mach numbers of 0.50 and 0.95 is significantly lower than the panel thickness

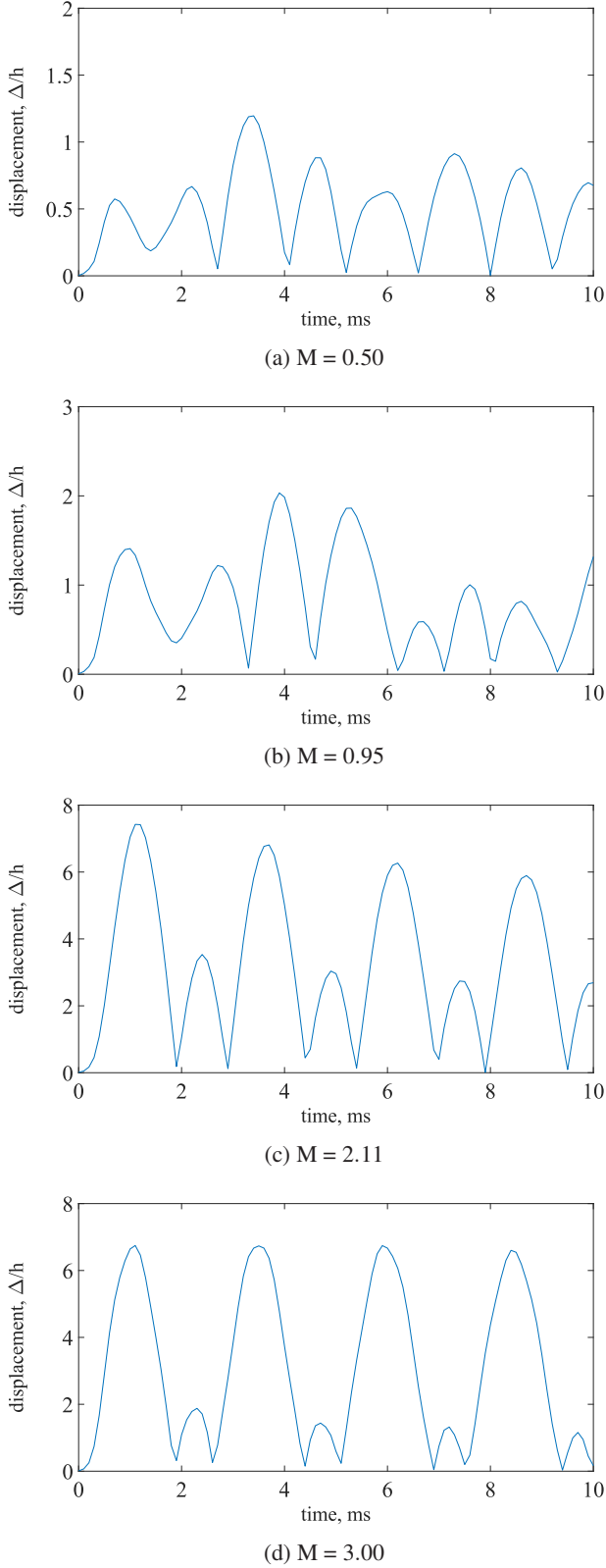


FIG. 10: Tip displacement for the first 10 ms for Mach numbers of 0.5, 0.95, 2.11 and 3.

of 1.02 mm , indicating that the flow does not have enough momentum to significantly deform the panel. For Mach 2 case, the deformation at the tip is two times the panel thickness which increases to three times when the flow Mach is increased to 3. This is attributed to the higher momentum of the flow leading to higher pressure loading which leads to increased panel bending and deformation.

To characterize the motion of the panel, the dominant frequency of the oscillation was calculated by performing an FFT of the time evolution of the displacement of the panel tip, shown previously in figure 10. The first peak in the frequency spectrum for each case is list in the table III below. A generic trend of increasing frequency with increasing Mach number is observed, with Mach 0.95 reporting the same frequency as the Mach 2.11. Higher flow momentum at higher Mach numbers results in increased pressure fluctuations leading to higher frequency pressure loading of the panel.

TABLE III: Thin-plate oscillation frequencies for initial transient conditions for the four Mach numbers under consideration.

Mach number	1 st Peak Hz
0.50	380
0.95	395
2.11	395
3.00	411

Figures 13a and b show the von Mises and shear stresses averaged over time along the length of the panel, respectively, for the four Mach numbers investigated in the paper. , figure 13a and the shear stress, figure 13b, are compared for changes with Mach number. An increase is observed in the von Mises stress from Mach 0.50 to 2.11, figure 13a: i, ii, iii, which then remains unchanged from 2.11 to 3.00, figure 13a: iii, iv. As discussed previously, increase in the flow Mach number leads to increase in the pressure loading which causes the panel to bend more resulting in the increased von Mises stress at the clamped edge. This trend suggests that the plate is at its highest von Mises stress for Mach numbers 2.11 and 3.00 and it can lead to significant non-linear deformation with increased loading by increasing the flow Mach number. For all four cases, the von Mises stress has maximum values close to the face attached to the backward facing step in figure 1. The maximum shear stress is observed at the base of the thin-plate, where it is attached to the backward facing step. The shear stress shows a consistent increase with increased loading, figure 13b: i to iv, with the cantilevered plate experiencing higher shear stresses along the middle of the bottom edge. As discussed earlier, the increase in Mach number results in increased pressure loading of the plate which results in higher shear stresses.

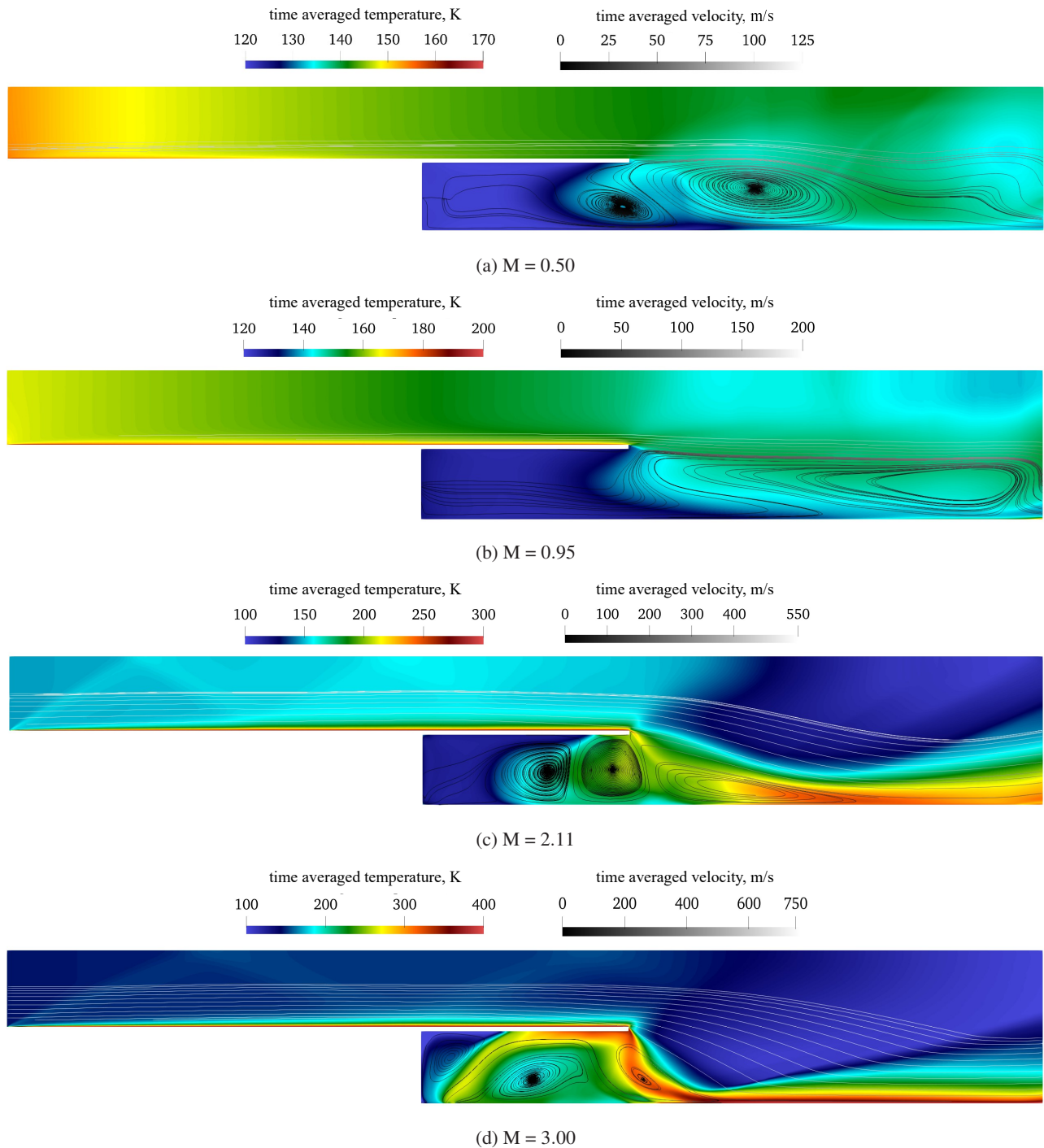


FIG. 11: Time-averaged temperature fields, overlaid with velocity streamlines for initial transient conditions.

B. Fully Started Conditions (up to 400 ms)

To capture fully-started conditions, the simulation is run for a physical time of 400 ms, or 1001 snapshots, with a time step of 4×10^{-4} . Mach 0.50, 2.11 and 3.00 run for the full simulation time while Mach 0.95 case runs only for 0.1 s or 250 snapshots.

1. Flow Behaviors

Flow evolution and the corresponding thin panel deflections for Ma 2.11 are shown in figure 14, for the times of 0, 50, 100, 200, 300 and 400 ms after the flow is initialized. The shear layer, separating the high-speed flow from the stationary air along the bottom section descends to the bottom wall trapping

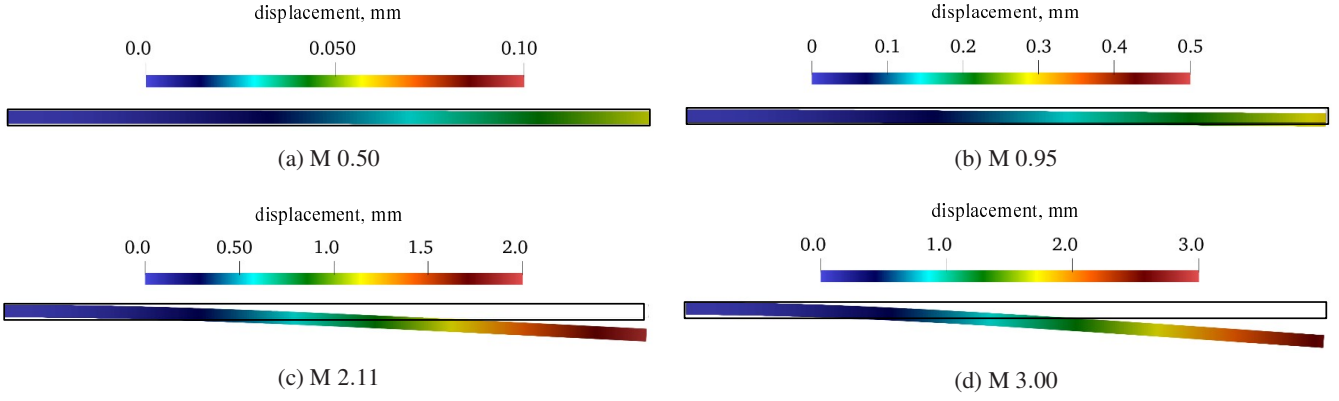


FIG. 12: Time averaged thin-panel displacements for all Mach numbers. Outline shows the initial undeformed panel.

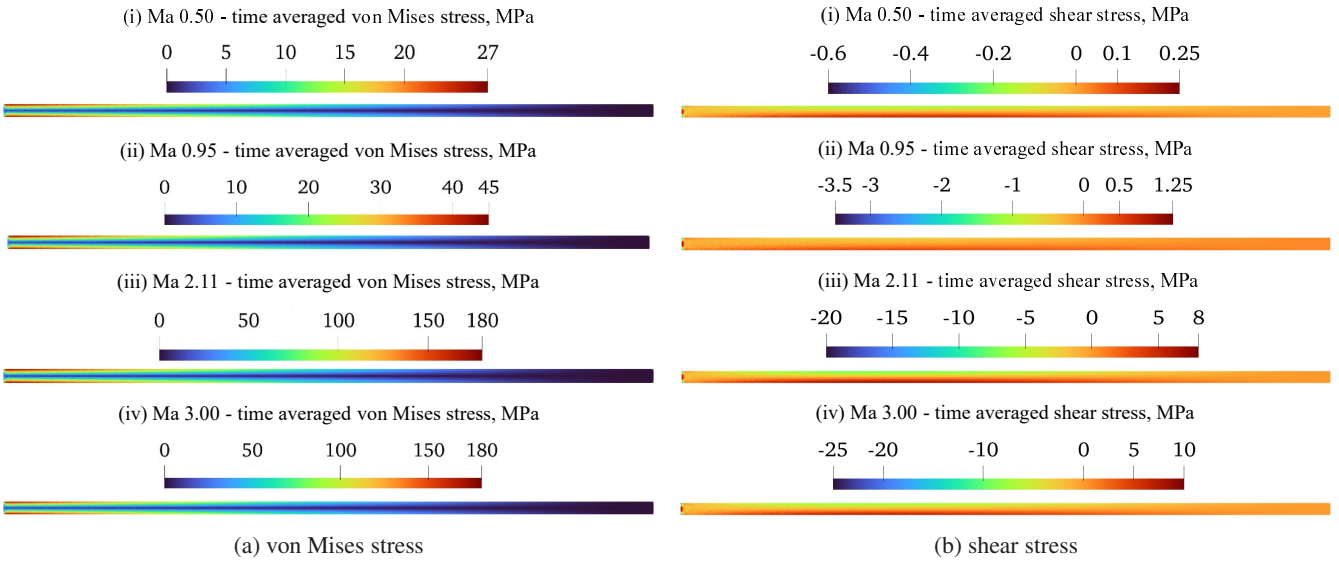


FIG. 13: Variation of von Mises and shear stress with Mach number for thin-aluminum plate for initial transient conditions.

a pocket of air behind it and under the thin panel by 50 *ms*, figure 14b. This prevents vortex shedding underneath the shear layer and leads to recirculation that increases the number or vortices formed, figure 14c-f. For subsequent times up to 400 *ms*, figure 14c-f, these vortices remain stationary and lead to viscous dissipation resulting in localized thermal hotspots that will be discussed later in this section.

The time averaged flow fields for fully started conditions are shown in figure 15. The shear layer separates the high speed flow region at the top with near stagnant flow at the bottom for Mach 0.50 and 0.95 cases, figure 15a, b. Large recirculating vortices are observed for these two cases, with possible low frequency vortex shedding due to no entrainment by the shear layer. The vortex that was attached to outer edge of the thin plate, but not to the shear layer for Mach 0.50, figure 9a, now gets attached to the shear layer, figure 15a. The shear layer completely restricts the high-speed flow to the upper region of the domain for Mach 0.50 and 0.95, and features such as the expansion fan, reattachment shock and recovery of

the boundary layer are not observed due to the non-attachment of the shear layer to the bottom wall, figure 1, for either case.

The shear layer gets attached to the bottom wall for Mach 2.11 and 3.00 trapping the vortices, figure 15c, d in an enclosed recirculation region as shown in figure 1. The structure of the vortices remains relative unchanged between transient, figure 9c, and fully-started, figure 15c, conditions for Mach 2.00. Additionally, two smaller vortices attached underneath the shear layer and before its reattachment to the bottom wall can be observed. For Mach 3.00, vortex structures similar to the Mach 2.11 case are observed, figure 15d, which are localized to the recirculation region, with two smaller vortices attached underneath the shear layer prior to its reattachment. Flow features shown in the schematic, figure 1, such as the expansion fan, reattachment shock, and recovering boundary layer are observed for Mach 2.11 and 3.00. The recovered boundary layer is thinner for the Mach 3.00 when compared to Mach 2.11 case, as the larger velocity magnitude after shear layer reattachment results in a larger velocity gradient for the

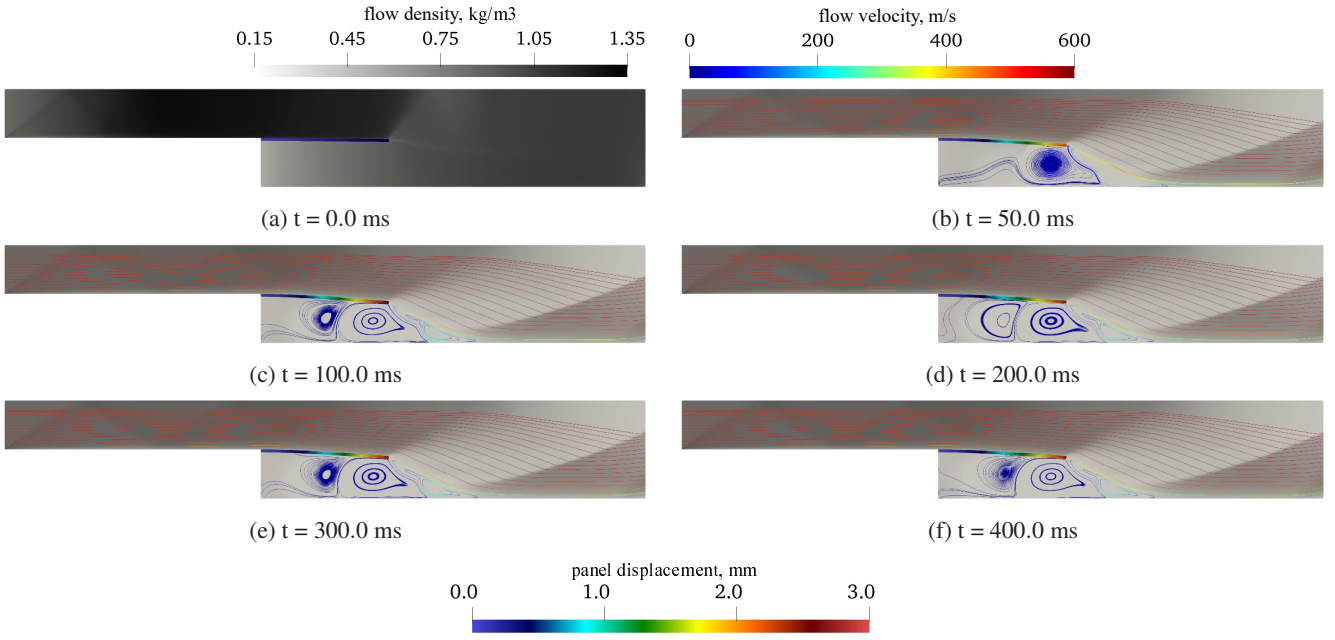


FIG. 14: Temporal evolution of Ma 2.11 flow, showing velocity streamlines on density contours and compliant panel displacement for fully started conditions.

Mach 3.00 case. These observations are also supported by temperature contours, figure 16.

The subsonic Mach 0.50, figure 16a, and transonic Mach 0.95, figure 16b, cases see an increase in temperature of the flowfield, including the high speed and low speed regions separated by the shear layer as compared to the transient conditions, figure 11a, b. The longer residence time for flow results in increased heating along the bottom wall of the inlet section and the thin plate top surface and a thicker thermal boundary layer. The sharp velocity and temperature gradients across the shear layer are present for fully-started conditions, with temperatures elevated due to viscous dissipation for longer times inside the recirculating vortices for both cases. While the temperature range remains unchanged for both Mach 0.50 and Mach 0.95 cases, the distribution is changed due to persistent viscous dissipation and thermal heating of the solid surfaces.

For the supersonic cases, Mach 2.11 and 3.00, the thermal boundary layer along the bottom wall of the inlet section experiences a much larger velocity and temperature gradient, resulting in increased temperatures, figure 16a, b. The stratification in temperature contours confirm the presence of the expansion fan the thin plate outer tip, and the reattachment shock further downstream along the bottom wall. Significant temperature increase is observed inside the vortices attached to the underneath of the shear layer and the thin-plate and trapped inside the recirculation region for both Mach 2.11 and 3.00. This is due to sustained viscous dissipation and entrapment of the vortices, which lead to increased heating of the fluid inside the recirculation region. Sustained dissipation can lead to excessive heating of the trapped gases inside the recirculation region with very high temperature increase leading to possible thermal failure of the thin-plate. The Mach 3.00 case

has higher temperatures within the vortices inside the recirculation region, as compared to the Mach 2.11 case. This can be attributed to the higher flow velocity of the Mach 3.00 case, which has relatively higher energy content leading to higher heating and dissipation rates. The thermal boundary layer for the Mach 2.11 case is recovers relatively earlier than the Mach 3.00 case. This is also be attributed to the higher flow velocity for the Mach 3.00 case which increases the length required for boundary layer recovery. Further increase in flow velocity can lead to extremely high temperatures, leading to ionization and chemical kinetic reactions that can lead to failure. These simulations are hence able to identify hot flow regions and zones for the flow configuration of figure 1, which can lead to extremely high temperature rises leading to the possibility of solid structure failure.

2. Panel Deformation and Stresses

The solid behavior is quantified with displacement-time plots to show the impact of Mach number in figure 17. The four cases exhibit different behavior for displacements with time and this is explored further with FFT analysis, stresses and modal decomposition to obtain dominant modes of vibration for analysis. The amplitude of displacement for the Mach 0.50 case initially decreases, but around 0.02 s it starts to increase again to stabilize to a maximum amplitude close to 2 times the plate thickness, figure 17a, after a time of 0.1 s. When the flow velocity is increased to Mach 0.95, the amplitude of oscillation of the thin plate steadily increases to 8 times the plate thickness, figure 17b, after which the excessive deformation leads to divergence of the simulation. This is as-

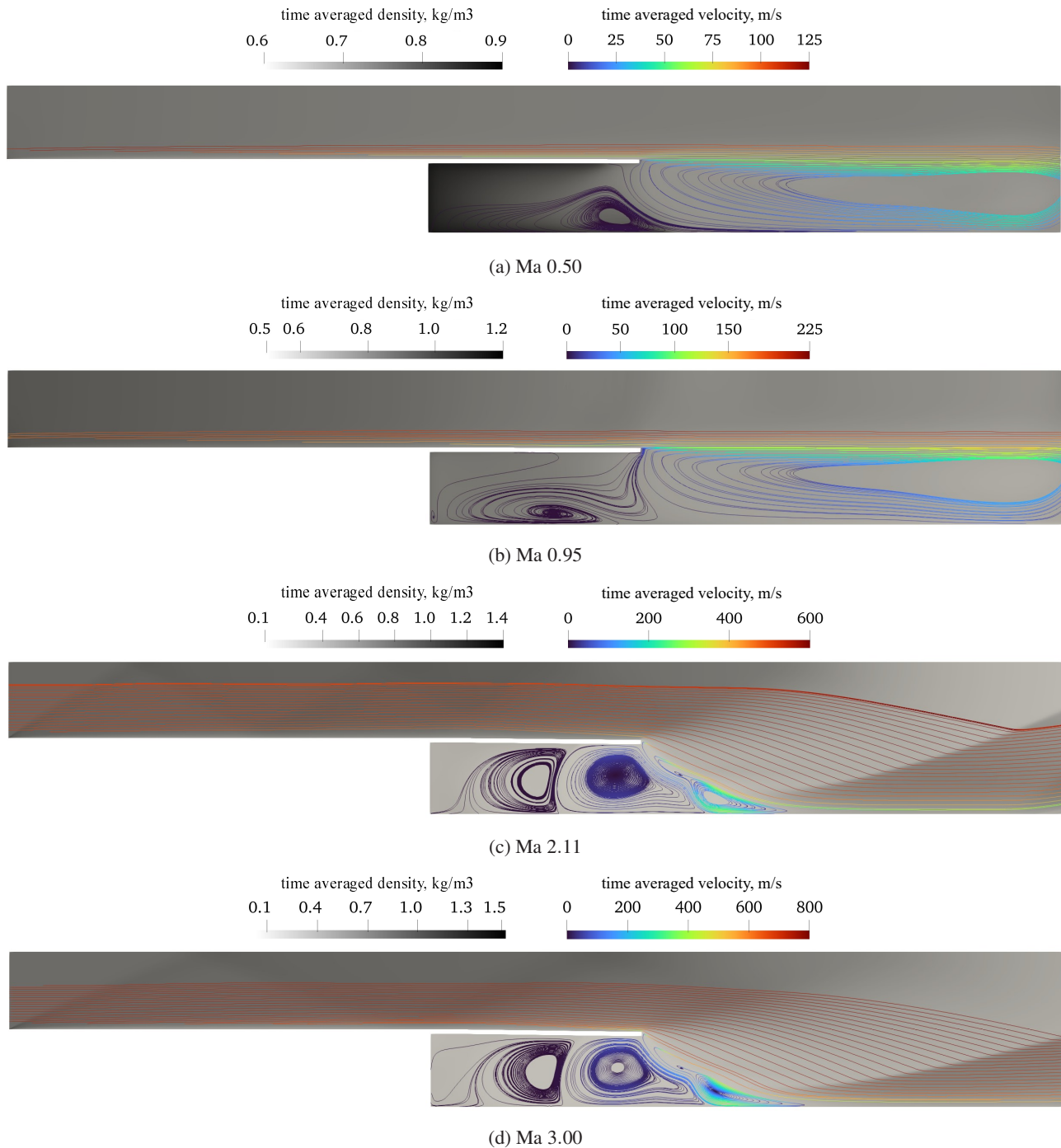


FIG. 15: Time-averaged density fields, overlaid with velocity streamlines for fully started conditions.

sumed as structural failure of the thin plate due to resonant behavior. For Mach 2.11 case, the tip displacement amplitudes rise to around 6 times the plate thickness, which are then stabilized around 0.2 s , figure 17c to $\frac{1}{5}$ times the plate thickness. The Mach 3.00 case shows a similar displacement-time plot, with the oscillations stabilized at smaller magnitudes than the Mach 2.11 case at 0.2 s , figure 17d. FFT analysis was conducted on the displacement-time series for the stabilized os-

cillations between 0.2 s and 0.4 s , for Mach 0.50, 2.11 and 3.00 cases.

FFT results are presented in figure 18a, c, d for Mach 0.50, 2.11 and 3.00 cases. For the Mach 0.95 case, FFT was conducted on the displacement-time data without truncation of the first 0.2 s , figure 18b. The peak frequencies are listed in table IV and frequencies lower than 300 Hz are not included in the discussion as this is the lower than the first natural fre-

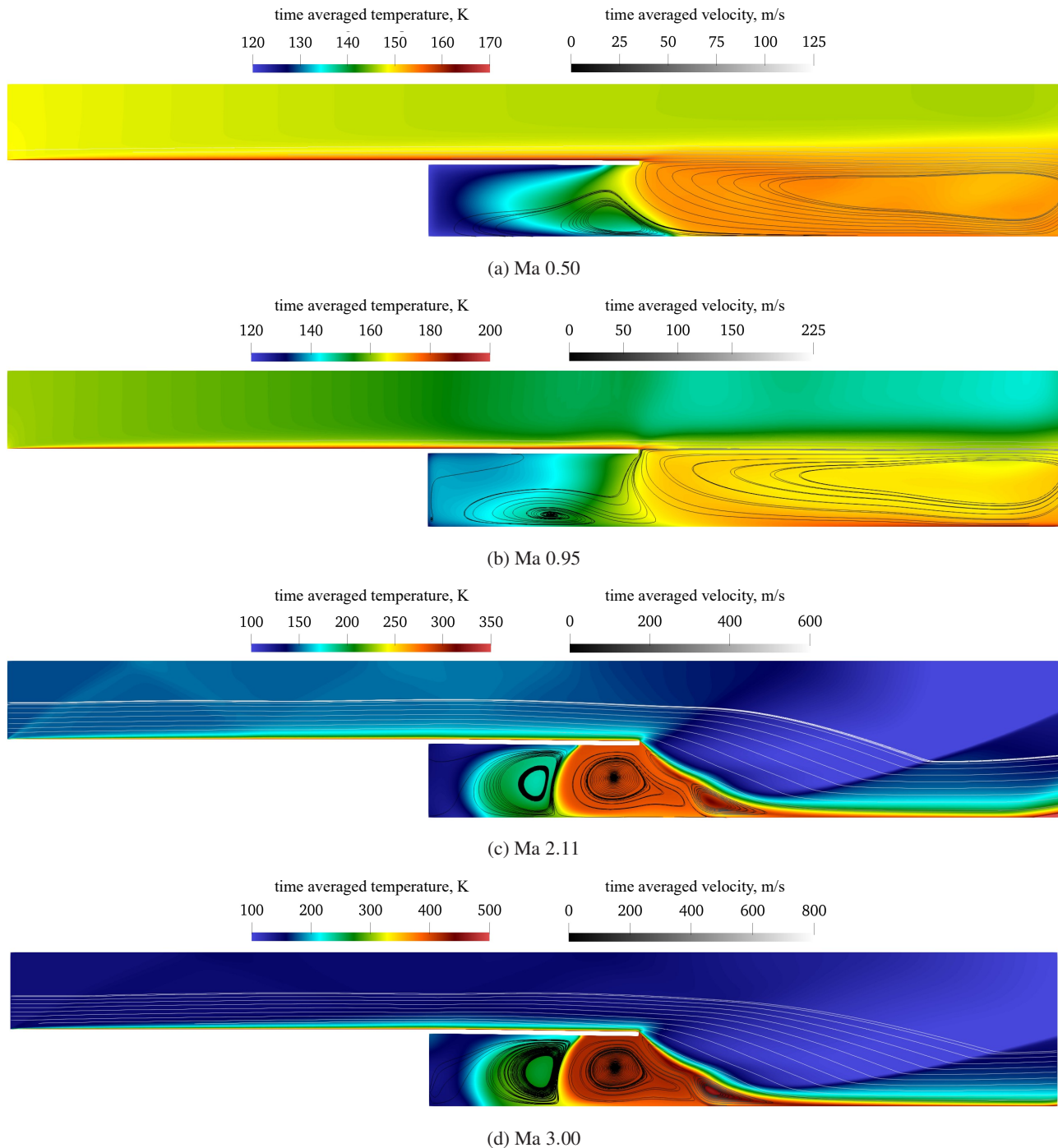


FIG. 16: Time-averaged temperature fields, overlaid with velocity streamlines for fully started conditions.

quency of the thin-plate. Mach 0.50 and 2.11 show a single peak at 676, figure 18a and 367 Hz, figure 18c, respectively, while Mach 3.00 shows two peaks with the first one at 971 Hz and a second peak at 367 Hz, figure 18d. This implies that increasing flow Mach number from 2.11 to 3.00 leads to a change in thin plate loading that results in it oscillating at a higher frequency. For Mach 0.95 case, 3 peaks are observed - at 740, 613 and 368 Hz, figure 18b. This suggests that a

natural mode of vibration is activated for this case leading to resonance and is followed by failure of the thin plate through excessive deformation by oscillations as shown by the plate tip displacement-time plot, figure 17d. This behavior is observed for transonic flows, where flutter phenomenon leading to resonance and failure has been frequently observed and reported in literature⁵⁴⁻⁵⁷.

Time averaged panel deformations are compared for all

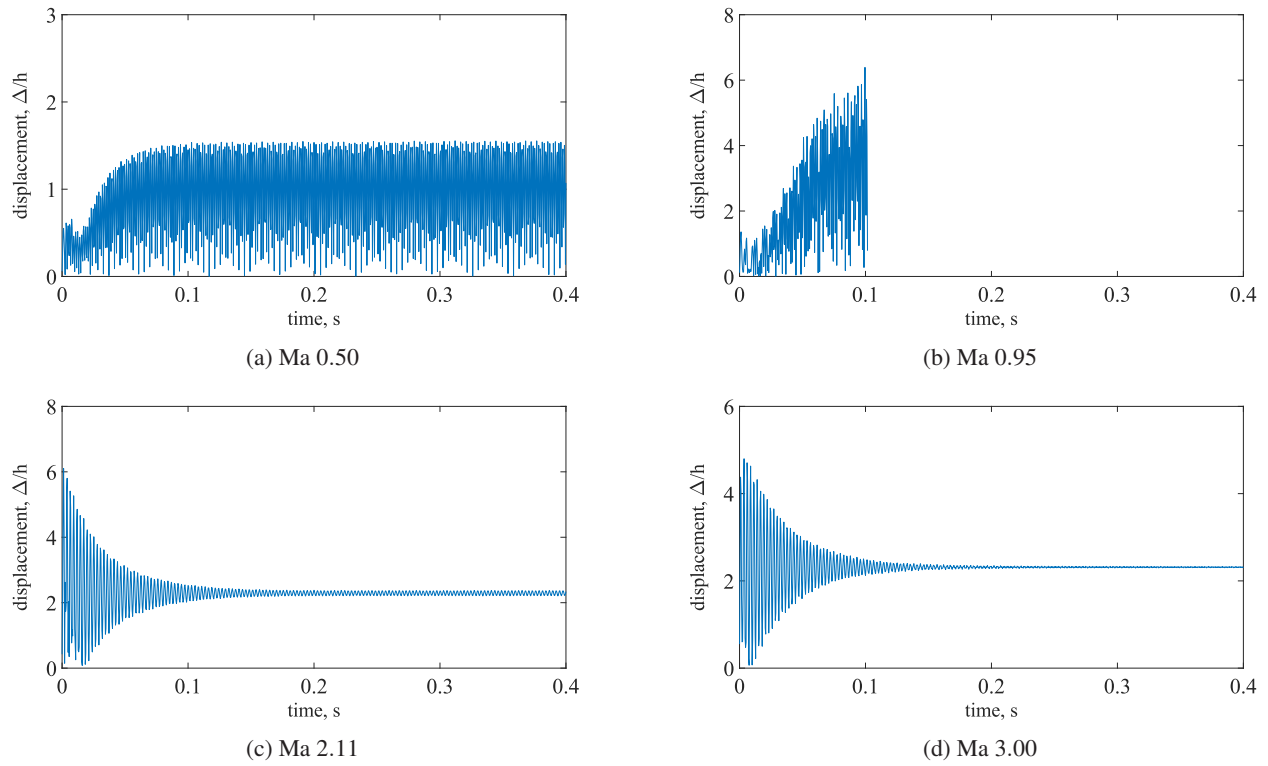


FIG. 17: Displacement-time plots for initial transient conditions for fully started conditions.

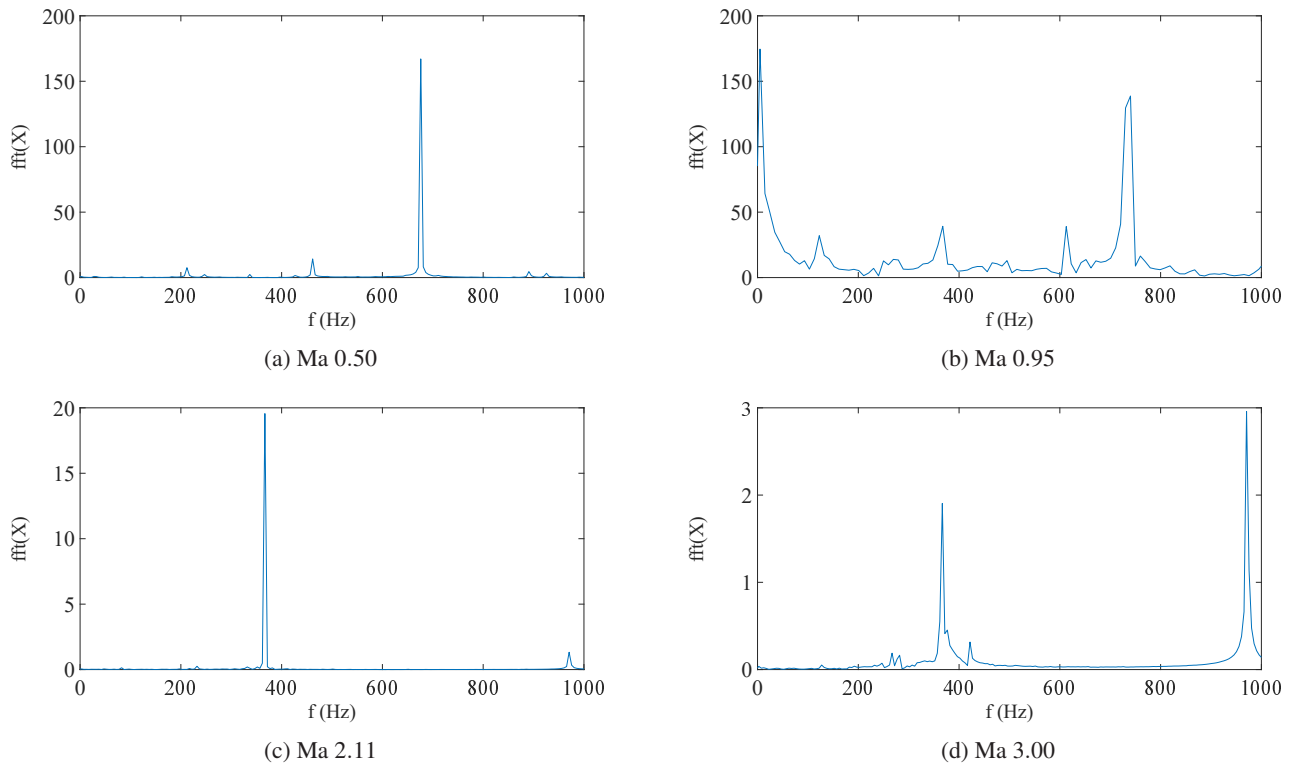


FIG. 18: FFT results for thin panel tip displacements for fully started conditions.

Mach	1 st Peak Hz	2 nd Peak Hz
0.50	676	
0.95	740	613, 368
2.11	367	
3.00	971	367

TABLE IV: Thin-plate oscillation frequencies for fully started conditions.

four Mach numbers in figure 19. An increase with increasing Mach number is observed. As discussed previously this is due to the higher pressure loading of the panel from the flow at higher Mach numbers.

von Mises stress for Mach 0.50, shows an increase in the peak value from 27, figure 13a: (i), to 50 *MPa*, figure 20a (i). The maximum shear stress also increases from 0.25 *MPa*, figure 13b: (i), to 0.60, figure 20b (i). This indicates that the plate stresses increase when the simulation is allowed to run for a longer time for the initial-transients to stabilize resulting in the fully-started conditions for Mach 0.50. However, for Mach 2.11 and 3.00, the peak value is reduced from 180 *MPa*, figure 13a: (iii), (iv), to 140 *MPa* for Mach 2.11, figure 20a: (iii), and to 150 *MPa*, figure 20a: (iv). This is due to the stabilization of the transient oscillations leading to relaxation in the plate. The shear stresses show a different trend with the peak value remaining unchanged for Mach 3.00 at 10 *MPa*, figure 20b: (iv), but lowering for Mach 2.11 from 10 *MPa* for initial transient conditions, figure 13b: (iii), to 8 *MPa* figure 20b: (iii), for fully started conditions. This implies that the thin plate is undergoing relaxation when the initial transient oscillations are stabilized and fully started conditions take over. Mach 0.95 is a unique case in this regard as the increase in von Mises stress from 45 *MPa* for the initial transient conditions, figure 13a: (ii), to 120 *MPa* for fully-started conditions, figure 20a: (ii), is comparatively much higher than the other three cases. As the thin-panel is oscillating at a natural frequency, the amplitude of oscillations keeps on consistently increasing as shown in figure 17b and this increase in amplitude results in a significantly large rise in the von Mises stress which leads to large amplitude oscillations and catastrophic failure from excessive deformation for the thin plate.

VI. CONCLUSIONS

FSI of a thin-flexible aluminum panel placed in high-speed air flow for initial-transient and fully-started conditions was investigated through high fidelity 2D numerical simulations.

Grid resolution of the flow domain has a significant impact on the thin-panel displacement, due to the better resolution of the boundary layer with the wall-model. This leads to accurate loading of the thin-plate, with improvements to the resulting plate displacements.

In this study, the standard logarithmic function was used for resolving the boundary layer flow, however there are other wall models that can significantly change the boundary layer

behavior. A comparative study of the various wall models that resolve the boundary layer behavior effecting the thin-plate loading FSI, will be investigated in a future study.

Initial transient behavior was consistent for flow features and solid behavior with experiments. Hotspots were identified inside the recirculation regions which show significant temperature rise for the supersonic cases with Mach 2.11 and 3.00, that could lead to even higher temperatures at those locations with continued high-speed flow.

The large oscillations due to pressure loading from the high-speed flow, along with the increased thermal loading from friction heating and viscous dissipation can lead to excessive deformation of the thin-plate. These initial transient simulations can be used as indicators for thin-panel failure if the simulation is allowed to run for longer times.

Running the simulations for times of 400 *ms* results in the stabilization of some of the observed transient behavior of the fluid and solid. The subsonic, Mach 0.50 and transonic Mach 0.95 cases see a significant rise in the thin-panel oscillation amplitude, with the oscillation amplitude getting stabilized and sustained for the subsonic case. However, for the transonic case, Mach 0.95, the amplitude steadily increases with solver divergence after 0.1 *s* indicating thin-panel failure due to resonant behavior. For the supersonic cases of Mach 2.11 and 3.00, the transient oscillations are stabilized with sustained oscillatory behavior which decreases in amplitude from Mach 2.11 to 3.00.

The supersonic Mach number cases see a very significant rise in temperatures in the fluid at the recirculation vortices, due to accumulation of thermal energy from viscous dissipation for a longer time. The high temperature hotspots in the fluid can result in significant thermal loading of the thin-panel which when sustained for longer times can lead to excessive panel deformation and ultimate failure when combined with pressure loading.

VII. ACKNOWLEDGMENTS

This research was supported by the DEVCOM Army Research Laboratory grant, W911NF-22-2-0058. The authors appreciate the High-Performance Computing Modernization Program (HPCMP) resources and support provided by the Department of Defense Supercomputing Resource Center (DSRC) as part of the 2022 Frontier Project, Large-Scale Integrated Simulations of Transient Aerothermodynamics in Gas Turbine Engines. The views and conclusions contained in this document are those of the authors and should not be interpreted as representing the official policies or positions, either expressed or implied, of the DEVCOM Army Research Laboratory or the U.S. Government. The U.S. Government is authorized to reproduce and distribute reprints for Government purposes notwithstanding any copyright notation herein.

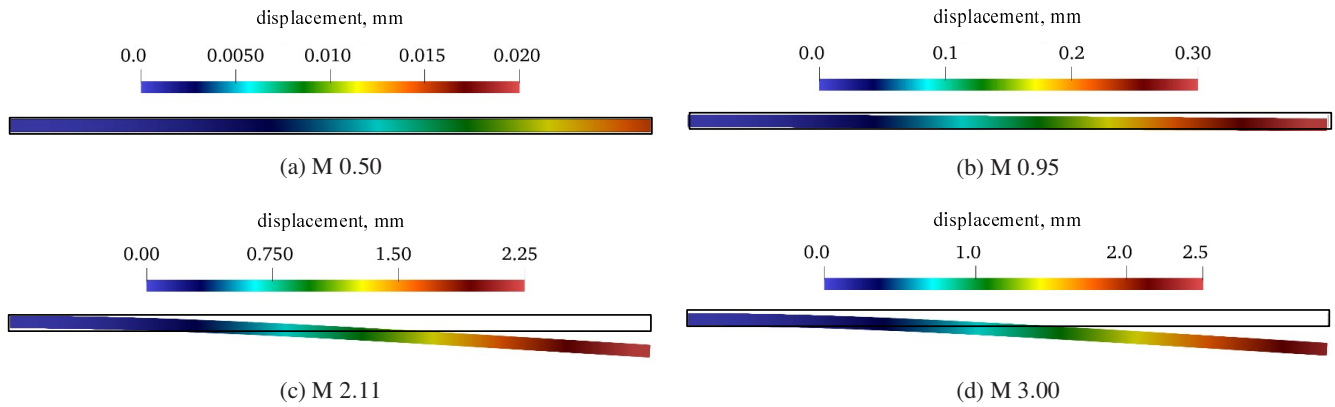


FIG. 19: Time averaged thin-panel displacements for all Mach numbers. Outline shows the initial undeformed panel.

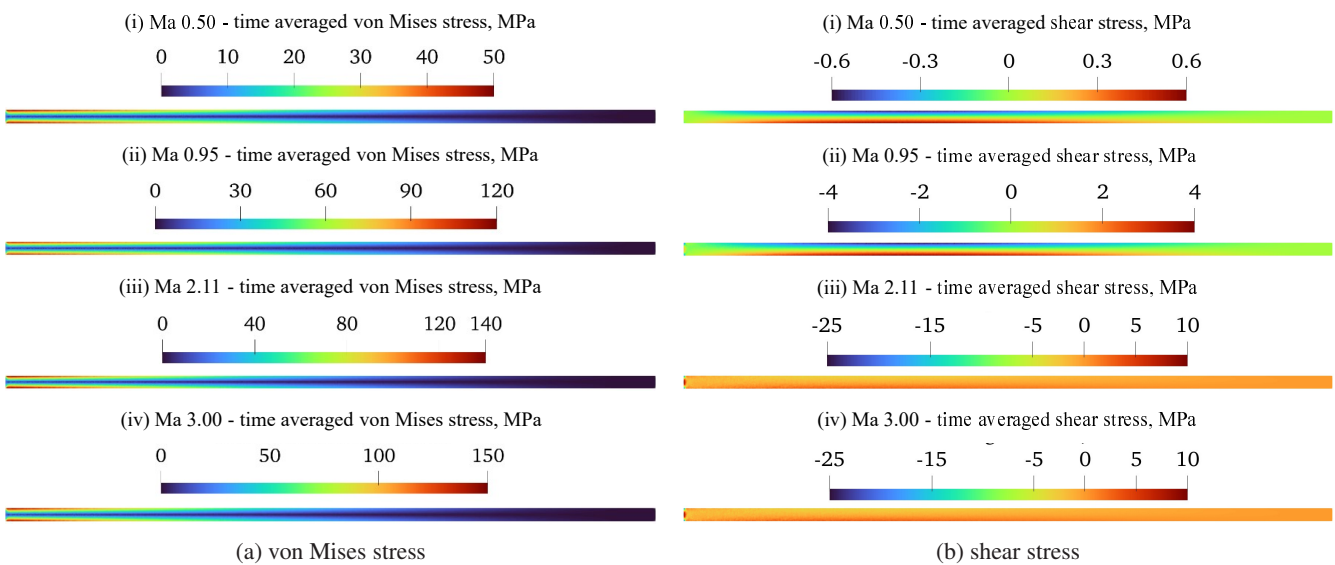


FIG. 20: Variation of von Mises and shear stress with Mach number for thin-flexible plate.

VIII. REFERENCES

- ¹E. H. Dowell and K. C. Hall, "Modeling of fluid-structure interaction," *Annual review of fluid mechanics* **33**, 445–490 (2001).
- ²B. E. Griffith and N. A. Patankar, "Immersed methods for fluid-structure interaction," *Annual review of fluid mechanics* **52**, 421–448 (2020).
- ³M. J. Smith, D. H. Hodges, and C. E. Cesnik, "Evaluation of computational algorithms suitable for fluid-structure interactions," *Journal of Aircraft* **37**, 282–294 (2000).
- ⁴G. Hou, J. Wang, and A. Layton, "Numerical methods for fluid-structure interaction—a review," *Communications in Computational Physics* **12**, 337–377 (2012).
- ⁵C. Wang, H. Tang, and X. Zhang, "Fluid-structure interaction of bio-inspired flexible slender structures: A review of selected topics," *Bioinspiration & biomimetics* **17**, 041002 (2022).
- ⁶M. Heil and A. L. Hazel, "Fluid-structure interaction in internal physiological flows," *Annual review of fluid mechanics* **43**, 141–162 (2011).
- ⁷C. Kleinstreuer, Z. Li, and M. Farber, "Fluid-structure interaction analyses of stented abdominal aortic aneurysms," *Annu. Rev. Biomed. Eng.* **9**, 169–204 (2007).
- ⁸M. Hirschhorn, V. Tchanchaleishvili, R. Stevens, J. Rossano, and A. Throckmorton, "Fluid-structure interaction modeling in cardiovascular medicine—a systematic review 2017–2019," *Medical engineering & physics* **78**, 1–13 (2020).
- ⁹C. Trivedi and M. J. Cervantes, "Fluid-structure interactions in francis turbines: A perspective review," *Renewable and Sustainable Energy Reviews* **68**, 87–101 (2017).
- ¹⁰A. Tijsseling, "Fluid-structure interaction in liquid-filled pipe systems: a review," *Journal of Fluids and Structures* **10**, 109–146 (1996).
- ¹¹D. M. Schuster, D. D. Liu, and L. J. Huttzell, "Computational aeroelasticity: success, progress, challenge," *Journal of Aircraft* **40**, 843–856 (2003).
- ¹²R. M. Ajaj, M. S. Parancheerivilakkathil, M. Amoozgar, M. I. Friswell, and W. J. Cantwell, "Recent developments in the aeroelasticity of morphing aircraft," *Progress in Aerospace Sciences* **120**, 100682 (2021).
- ¹³I. Garrick, "Aeroelasticity-frontiers and beyond," *Journal of Aircraft* **13**, 641–657 (1976).
- ¹⁴P. P. Friedmann, "Renaissance of aeroelasticity and its future," *Journal of aircraft* **36**, 105–121 (1999).
- ¹⁵P. P. Friedmann, "Rotary-wing aeroelasticity: Current status and future trends," *AIAA journal* **42**, 1953–1972 (2004).
- ¹⁶J. Redding, N. Plewacki, H. Ganti, L. Bravo, and P. Khare, "Analysis of thermochemical non-equilibrium hypersonic

- flow over a waverider with uncertainty quantification,” arXiv preprint arXiv:2405.15875 (2024), <https://doi.org/10.48550/arXiv.2405.15875>.
- ¹⁷J. Redding, J. Gamertsfelder, L. Bravo, and P. Khare, “Thermochemical non-equilibrium hypersonic flow over a rectangular cavity embedded on a compression ramp,” *Physics of Fluids* **35** (2023), <https://doi.org/10.1063/5.0172435>.
- ¹⁸J. Gamertsfelder, J. Redding, L. Bravo, and P. Khare, “Flow and heat transfer characteristics of aerothermodynamic loading on a double cone at mach 12,” in *Heat Transfer Summer Conference*, Vol. 87165 (American Society of Mechanical Engineers, 2023) p. V001T06A001.
- ¹⁹M. Kamin, J. Eblin, and P. Khare, “The nexgen burner: Non-reacting gaseous and spray dynamics,” *Physics of Fluids* **35** (2023), <https://doi.org/10.1063/5.0169823>.
- ²⁰M. Kamin, L. Bravo, and P. Khare, “The nexgen burner: Analysis of turbulent fuel-air mixing,” in *Turbo Expo: Power for Land, Sea, and Air*, Vol. 87950 (American Society of Mechanical Engineers, 2024) p. V03BT04A077.
- ²¹M. Kamin, N. Plewacki, R. Koneru, L. Bravo, P. Khare, R. Powers, K. Miki, F. Ham, and M. Senga, “Large eddy simulation of turbulent reacting flow in a pressurized annular combustor,” in *Turbo Expo: Power for Land, Sea, and Air*, Vol. 87943 (American Society of Mechanical Engineers, 2024) p. V03AT04A072.
- ²²M. Tripathi, H. Ganti, and P. Khare, “Interactions between shock waves and liquid droplet clusters: Interfacial physics,” *Journal of Fluids Engineering* **144**, 101401 (2022).
- ²³J. P. Redding and P. Khare, “A computational study on shock induced deformation, fragmentation and vaporization of volatile liquid fuel droplets,” *International Journal of Heat and Mass Transfer* **184**, 122345 (2022).
- ²⁴M. Kamin and P. Khare, “The effect of weber number on spray and vaporization characteristics of liquid jets injected in air crossflow,” *Journal of Fluids Engineering* **144**, 061108 (2022).
- ²⁵S. Valencia, A. Mendiburu, L. Bravo, P. Khare, and C. Celis, “Flow-field analysis and performance assessment of rotating detonation engines under different number of discrete inlet nozzles,” *Applications in Energy and Combustion Science*, 100296 (2024).
- ²⁶F. Ilacanchi, S. Valencia, C. Celis, A. Mendiburu, L. Bravo, and P. Khare, “Numerical study of distorted tulip flame propagation in confined systems,” arXiv preprint arXiv:2309.05893 (2023), <https://doi.org/10.48550/arXiv.2309.05893>.
- ²⁷B. T. Sullivan, D. J. Bodony, T. Whalen, and S. Laurence, “Direct simulation of fluid-structure interaction in a hypersonic compression-ramp flow,” *AIAA journal* **58**, 4848–4865 (2020).
- ²⁸J. Hoy and I. Bernejo-Moreno, “Fluid-structural coupling of an impinging shock–turbulent boundary layer interaction at mach 3 over a flexible panel,” *Flow* **2**, E35 (2022).
- ²⁹J. Boustani, M. F. Barad, C. C. Kiris, and C. Brehm, “An immersed interface methodology for simulating supersonic spacecraft parachutes with fluid–structure interaction,” *Journal of Fluids and Structures* **114**, 103742 (2022).
- ³⁰G. Currao, A. J. Neely, R. Buttsworth, and R. Choudhury, “Measurement and simulation of hypersonic fluid-structural interaction on a cantilevered plate in a mach 6 flow,” in *15th Dynamics Specialists Conference* (American Institute of Aeronautics and Astronautics, 2016).
- ³¹G. M. D. Currao, A. J. Neely, C. M. Kennell, S. L. Gai, and D. R. Buttsworth, “Hypersonic fluid–structure interaction on a cantilevered plate with shock impingement,” *AIAA Journal* **57**, 4819–4834 (2019).
- ³²G. M. Currao, L. P. McQuellin, A. J. Neely, F. Zander, D. Buttsworth, J. J. McNamara, and I. Jahn, “Oscillating shock impinging on a flat plate at mach 6,” in *AIAA Aviation 2019 Forum* (American Institute of Aeronautics and Astronautics, 2019) pp. 1–26.
- ³³G. K. Bojan, J. C. Dutton, and G. S. Elliott, “Fluid/structure interaction of cantilevered plate in supersonic separated flow,” *AIAA Journal* **60**, 6726–6738 (2022).
- ³⁴S. Willems, A. Gülhan, and B. Esser, “Shock induced fluid-structure interaction on a flexible wall in supersonic turbulent flow,” in *Progress in Flight Physics*, edited by P. Reijasse, D. Knight, M. Ivanov, and I. Lipatov (EDP Sciences, 2013) pp. 285–308.
- ³⁵Z. B. Riley, R. A. Perez, G. W. Bartram, S. M. Spottswood, B. P. Smarslok, and T. J. Bebernis, “Aerothermoelastic experimental design for the aedc/vkf tunnel c: Challenges associated with measuring the response of flexible panels in high-temperature, high-speed wind tunnels,” *Journal of Sound and Vibration* **441**, 96–105 (2019).
- ³⁶S. M. Spottswood, T. J. Bebernis, T. G. Eason, R. A. Perez, J. M. Donbar, D. A. Ehrhardt, and Z. B. Riley, “Exploring the response of a thin, flexible panel to shock-turbulent boundary-layer interactions,” *Journal of Sound and Vibration* **443**, 74–89 (2019).
- ³⁷S. J. Peltier, B. E. Rice, J. Szmodis, D. R. Ogg, J. W. Hofferth, M. E. Sellers, and A. J. Harris, “Aerodynamic response to a compliant panel in mach 4 flow,” in *AIAA Aviation 2019 Forum* (American Institute of Aeronautics and Astronautics, 2019) pp. 1–1.
- ³⁸T. J. Whalen, A. G. Schöneich, S. J. Laurence, B. T. Sullivan, D. J. Bodony, M. Freydin, E. H. Dowell, and G. M. Buck, “Hypersonic fluid–structure interactions in compression corner shock-wave/boundary-layer interaction,” *AIAA Journal* **58**, 4090–4105 (2020).
- ³⁹R. Ravichandran, M. Gramola, and P. J. Bruce, “Simultaneous pressure and displacement measurements on a 3d flexible surface in a supersonic flow,” in *AIAA Scitech 2020 Forum*, Vol. 1 PartF (American Institute of Aeronautics and Astronautics, 2020).
- ⁴⁰Z. B. Riley, R. A. Perez, and D. A. Ehrhardt, “Response of a thin panel to aerothermal loading at mach 6,” *AIAA Journal* **59**, 3787–3793 (2021).
- ⁴¹K. R. Brouwer, R. A. Perez, T. J. Bebernis, S. M. Spottswood, and D. A. Ehrhardt, “Experiments on a thin panel excited by turbulent flow and shock/boundary-layer interactions,” *AIAA Journal* **59**, 2737–2752 (2021).
- ⁴²D. Daub, S. Willems, and A. Gülhan, “Experiments on aerothermoelastic fluid–structure interaction in hypersonic flow,” *Journal of Sound and Vibration* **531**, 116714–116714 (2022).
- ⁴³K. R. Brouwer, R. A. Perez, T. J. Bebernis, S. M. Spottswood, and D. A. Ehrhardt, “Evaluation of reduced-order aeroelastic simulations for shock-dominated flows,” *Journal of Fluids and Structures* **108**, 103429–103429 (2022).
- ⁴⁴K. R. Brouwer, R. Perez, T. J. Bebernis, and S. M. Spottswood, “Surface pressure measurements and predictions in shock-dominated flows,” in *AIAA AVIATION 2023 Forum* (American Institute of Aeronautics and Astronautics, 2023).
- ⁴⁵T. D. Economou, F. Palacios, S. R. Copeland, T. W. Lukaczyk, and J. J. Alonso, “Su2: An open-source suite for multiphysics simulation and design,” *AIAA Journal* **54**, 828–846 (2016).
- ⁴⁶A. W. Vreman, B. J. Geurts, and J. G. M. Kuerten, “Subgrid-modelling in les of compressible flow,” in *Direct and Large-Eddy Simulation I: Selected papers from the First ERCOFTAC Workshop*, edited by P. R. Voke, L. Kleiser, and J.-P. Chollet (Springer Netherlands, Dordrecht, 1994) pp. 133–144.
- ⁴⁷J. Smagorinsky, “General circulation experiments with the primitive equations,” *Monthly Weather Review* **91**, 99–164 (1963).
- ⁴⁸H. Reichardt, “Vollständige darstellung der turbulenten geschwindigkeitsverteilung in glatten leitungen,” *ZAMM - Journal of Applied Mathematics and Mechanics / Zeitschrift für Angewandte Mathematik* **21**, 293–309 (1951).
- ⁴⁹D. B. Spalding *et al.*, “A single formula for the law of the wall,” *Journal of Applied mechanics* **28**, 455–458 (1961).
- ⁵⁰A. J. Musker, “Explicit expression for the smooth wall velocity distribution in a turbulent boundary layer,” *AIAA Journal* **17**, 655–657 (1979).
- ⁵¹J. Bonet and R. D. Wood, *Nonlinear Continuum Mechanics for Finite Element Analysis* (Cambridge University Press, 2008).
- ⁵²R. Sanchez, R. Palacios, T. D. Economou, H. L. Kline, J. J. Alonso, and F. Palacios, “Towards a fluid-structure interaction solver for problems with large deformations within the open-source su2 suite,” in *57th AIAA/ASCE/AHS/ASC Structures, Structural Dynamics, and Materials Conference* (American Institute of Aeronautics and Astronautics, 2016).
- ⁵³R. Sanchez, H. L. Kline, D. Thomas, A. Variyar, M. Righi, T. D. Economou, J. J. Alonso, R. Palacios, G. Dimitriadis, V. Terrapon, and A. Sanchez, “Assessment of the fluid-structure interaction capabilities for aeronautical applications of the open-source solver su2,” in *VII European Congress on Computational Methods in Applied Sciences and Engineering* (Institute of Structural Analysis and Antiseismic Research, 2016) pp. 1–32.
- ⁵⁴J. M. Hedgepeth, “Flutter of rectangular simply supported panels at high supersonic speeds,” *Journal of the Aeronautical Sciences* **24**, 563–573 (1957).
- ⁵⁵C. J. Borland and D. P. Rizzetta, “Nonlinear transonic flutter analysis,” *AIAA Journal* **20**, 1606–1615 (1982).
- ⁵⁶G. Davis and O. Bendiksen, “Transonic panel flutter,” in *34th Structures, Structural Dynamics and Materials Conference* (Ameri-

can Institute of Aeronautics and Astronautics, 1992).

⁵⁷C. Mei, K. Abdel-Motagaly, and R. Chen, "Review of non-linear panel flutter at supersonic and hypersonic speeds,"

Applied Mechanics Reviews **52**, 321–332 (1999).